

# Electromagnetic Excitation of Nucleon Resonances

L. Tiator<sup>1,a</sup>, D. Drechsel<sup>1,b</sup>, S.S. Kamalov<sup>2,c</sup> and M. Vanderhaeghen<sup>1,d</sup>

<sup>1</sup> Institut für Kernphysik, Johannes Gutenberg-Universität, D-55099 Mainz, Germany

<sup>2</sup> Laboratory of Theoretical Physics, JINR Dubna, 141980 Moscow Region, Russia

**Abstract.** Recent progress on the extraction of electromagnetic properties of nucleon resonance excitation through pion photo- and electroproduction is reviewed. Cross section data measured at MAMI, ELSA, and CEBAF are analyzed and compared to the analysis of other groups. On this basis, we derive longitudinal and transverse transition form factors for most of the four-star nucleon resonances. Furthermore, we discuss how the transition form factors can be used to obtain empirical transverse charge densities. Contour plots of the thus derived densities are shown for the Delta, Roper,  $S_{11}$ , and  $D_{13}$  nucleon resonances.

## 1 Introduction

Our knowledge about the excitation spectrum of the nucleon was originally provided by elastic pion-nucleon scattering. All the resonances listed in the Particle Data Tables (PDG) [1] were identified by partial-wave analyses of this process with both Breit-Wigner and pole extraction techniques. In PDG the nucleon resonances  $N^*$  and  $\Delta$  are given a status from one-star for a ‘poor evidence of existing’ up to four-star for a ‘certain existence’, where ‘properties are at least fairly well explored’. In Fig. 1 we show part of the PDG summary table including only three- and four-star resonances up to a mass of 2 GeV. But out of 13 four-star resonances, only 5 are listed with also four stars in the  $N\gamma$  channel. For others the e.m. properties are at best only approximately known. From partial wave analyses we know the resonance masses, widths, pole positions, and branching ratios into the  $\pi N$  and  $\pi\pi N$  channels. These are reliable parameters for the four-star resonances, with only few exceptions. In particular, there remains some doubt about the structure of two prominent resonances, the Roper  $P_{11}(1440)$ , which appears unusually broad, and the  $S_{11}(1535)$  whose pole position can not be uniquely determined because its closeness to the  $\eta N$  threshold. In Figs. 2-3 we have mapped the  $P_{33}$  and  $P_{11}$  partial waves in the complex energy plane, as derived from an analysis within the Dubna-Mainz-Taipei dynamical meson-exchange model [2,3]. In both cases, the plots show 3-4 poles for imaginary values of  $W$  from zero down to about  $-250$  MeV. The residues of the poles are proportional to the size of the white disks in the figures. However, one should keep in mind that the

<sup>a</sup> e-mail: [tiator@kph.uni-mainz.de](mailto:tiator@kph.uni-mainz.de)

<sup>b</sup> e-mail: [drechsel@kph.uni-mainz.de](mailto:drechsel@kph.uni-mainz.de)

<sup>c</sup> e-mail: [kamalov@theor.jinr.ru](mailto:kamalov@theor.jinr.ru)

<sup>d</sup> e-mail: [marcvdh@kph.uni-mainz.de](mailto:marcvdh@kph.uni-mainz.de)

Particle	$L_{2I \cdot 2J}$	Overall status	$N\pi$	$N\gamma$
$N(939)$	$P_{11}$			
$N(1440)$	$P_{11}$	****	****	***
$N(1520)$	$D_{13}$	****	****	****
$N(1535)$	$S_{11}$	****	****	***
$N(1650)$	$S_{11}$	****	****	***
$N(1675)$	$D_{15}$	****	****	****
$N(1680)$	$F_{15}$	****	****	****
$N(1700)$	$D_{13}$	***	***	**
$N(1710)$	$P_{11}$	***	***	***
$N(1720)$	$P_{13}$	****	****	**
$\Delta(1232)$	$P_{33}$	****	****	****
$\Delta(1600)$	$P_{33}$	***	***	**
$\Delta(1620)$	$S_{31}$	****	****	***
$\Delta(1700)$	$D_{33}$	****	****	***
$\Delta(1905)$	$F_{35}$	****	****	***
$\Delta(1910)$	$P_{31}$	****	****	*
$\Delta(1920)$	$P_{33}$	***	***	*
$\Delta(1930)$	$D_{35}$	***	***	**
$\Delta(1950)$	$F_{37}$	****	****	****

**Fig. 1.**  $N$  and  $\Delta$  resonances with overall status of three and four stars below 2 GeV. Taken in part from *Review of Particle Physics* [1]

influence of a pole on the physical region decreases rapidly with the distance from the real axis.

On the basis of these relatively firm grounds, additional information can be obtained for the electromagnetic (e.m.)  $\gamma NN^*$  couplings through meson photo- and electroproduction. By far, the main source for resonance structure is pion production, but in some cases with a small  $\pi N$  branching ratio, also  $\eta$ ,  $\pi\pi$ ,  $K$ ,  $\rho$ ,  $\omega$ , etc. production can give valuable information. A typical such example is the  $S_{11}(1535)$  resonance, which is located close to the  $\eta N$  threshold and strongly coupled to this channel.

Here we will concentrate on the analysis of pion photo- and electroproduction. The  $\gamma N$  couplings can be given in terms of electric, magnetic, and Coulomb transition moments or, alternatively, as helicity amplitudes. The PDG lists only the helicity amplitudes  $A_{1/2}$  and  $A_{3/2}$  for real photons. These amplitudes are real numbers, which are determined at the Breit-Wigner position of a given resonance. In electroproduction, an additional longitudinal amplitude  $S_{1/2}(Q^2)$  can be determined and all three amplitudes become functions of  $Q^2$ . In particular for the  $N \rightarrow \Delta$  transition, a set of 3 Sachs form factors ( $G_E^*$ ,  $G_M^*$ ,  $G_C^*$ ) is often introduced and, most recently, also a set of covariant Dirac form factors ( $F_1^{NN^*}$ ,  $F_2^{NN^*}$ ,  $F_3^{NN^*}$ ) has been used, especially for comparison with lattice QCD and as a source to derive transverse transition densities in the light-front frame. A general derivation of  $NN^*$  transition form factors for arbitrary spin and parity states can be found in the paper by Devenish, Eisenschitz, and Körner [4].

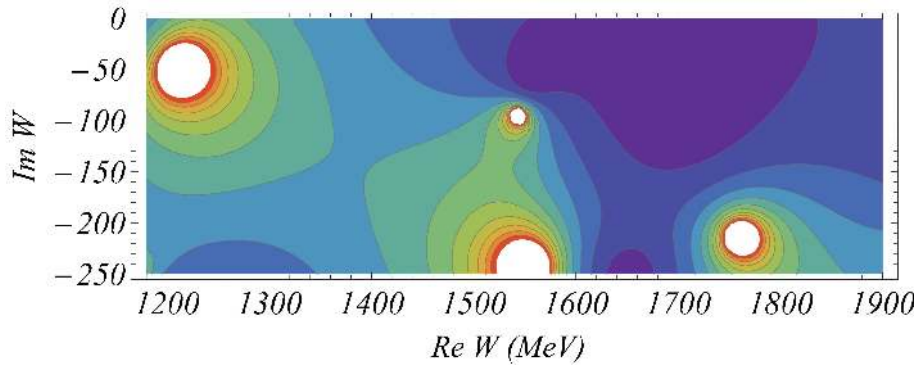


**Fig. 2.** Contour plot of  $|T_{\pi N}(W)|$  for the  $P_{33}$  partial wave in the Dubna-Mainz-Taipei model [2,3]. The light and dark regions show poles and zeroes, respectively, in the first unphysical sheet of  $W$ . Three of the four poles seen in this plot belong to the  $P_{33}(1232)$ ,  $P_{33}(1600)$ , and  $P_{33}(1920)$  resonances listed in PDG. The fourth pole at  $(1554 - 243i)$  MeV has no noticeable influence for  $\pi N$  in the physical region.

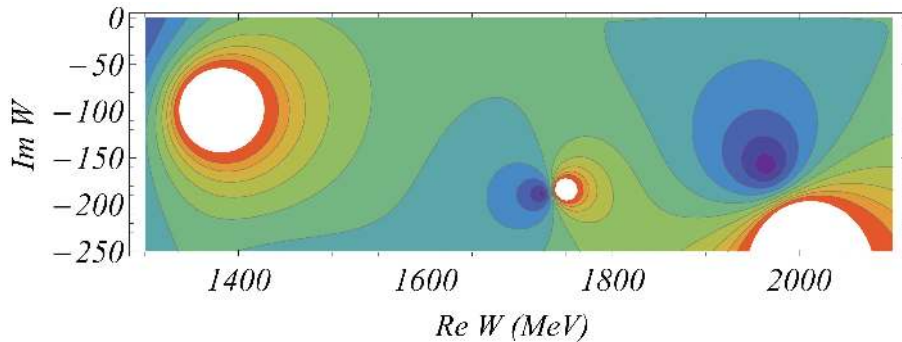


**Fig. 3.** Same as in Fig. 2 for the  $P_{11}$  partial wave. The three poles seen in this plot belong to the  $P_{11}(1440)$ ,  $P_{11}(1710)$ , and  $P_{11}(2100)$  resonances listed in PDG.

Until about 10 years ago, information on the transition form factors (FF) at finite  $Q^2$  was very scarce and, in particular, nonexistent for the longitudinal form factor. The best knowledge we had was on the magnetic  $N \rightarrow \Delta(1232)$  form factor  $G_M^*(Q^2)$ , which was fairly well known up to about  $Q^2 = 10 \text{ GeV}^2$ . This is the only  $NN^*$  transition form factor which can be directly measured in inclusive electron scattering [5,6,7,8,9,10,11,12] because of the very strong  $M1$  transition to the isolated  $\Delta(1232)$  resonance.

The new era started with  $\pi^0$  electroproduction experiments at Mainz [13,14,15], Bonn [16,17], and Bates [18,19] in search for the small  $E2$  and  $C2$  transition form factors for  $N \rightarrow \Delta$  and the determination of the  $E/M$  and  $S/M$  ratios.

Already in the mid-nineties, the resonant multipoles (FFs at  $Q^2 = 0$ ) and in particular the  $E/M$  ratio were investigated in experimental programs at MAMI in Mainz [20] and LEGS in Brookhaven [21]. In Fig. 4 we display the  $P_{33}$  amplitudes as derived from unpolarized differential cross sections and photon beam asymmetries measured with MAMI B for both  $p(\gamma, \pi^0)p$  and  $p(\gamma, \pi^+)n$ . The shown results are based

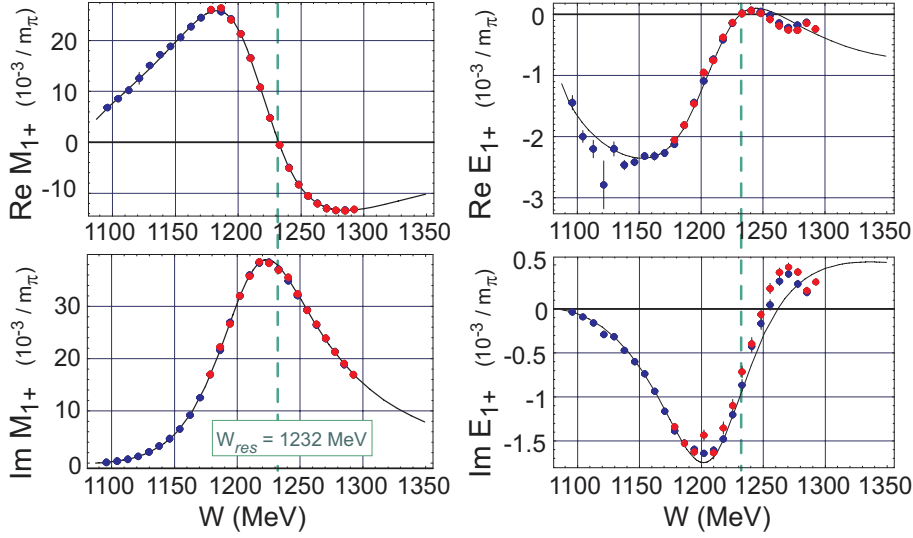


**Fig. 4.** Pion photoproduction multipoles  $M_{1+}$  and  $E_{1+}$  in the  $P_{33}$  channel. The red and blue data points are mostly overlapping and are obtained from the analyses of Beck et al. [20,24] and Hanstein et al. [22,23], respectively. The solid lines show the energy-dependent dispersion theoretical analysis of Hanstein et al. [23].

on a model-independent partial wave analysis as performed by the Mainz group during the years 1995-2000. With the well justified assumptions of the Watson theorem (due to unitarity) and the neglect of non-Born D and higher wave contributions, the measurement of only 2 observables for each channel was sufficient to determine the partial waves without any model input. From the  $E_{1+}^{3/2}$  and  $M_{1+}^{3/2}$  multipoles, the following  $\Delta(1232)$  resonance properties were obtained [20,24,22,23]:

- e.m. transition moments and  $R_{EM}$  ratio at  $W_{res} = 1232$  MeV

$$\mu_{N\Delta} = (3.46 \pm 0.03) \mu_N, \quad (1)$$

$$Q_{N\Delta} = -(0.0846 \pm 0.0033) \text{ fm}^2, \quad (2)$$

$$R_{EM} = -(2.5 \pm 0.1_{stat.} \pm 0.2_{syst.}) \% \quad (3)$$

- pole position and residues at  $W_{pole} = M_p - i/2 \Gamma_p$

$$M_p = (1212 \pm 1) \text{ MeV}, \quad (4)$$

$$\Gamma_p = (99 \pm 2) \text{ MeV}, \quad (5)$$

$$r(M1) = 21.16 \cdot e^{-i 27.5^\circ} 10^{-3}/m_\pi, \quad (6)$$

$$r(E2) = 1.23 \cdot e^{-i 154.7^\circ} 10^{-3}/m_\pi, \quad (7)$$

$$R_\Delta = \frac{r(E2)}{r(M1)} = -0.035 - 0.046 i. \quad (8)$$

During the last decade, a big step forward was made at JLab [25,26,27,28,29,30,31,32,33,34] by a series of experiments measuring electroproduction of  $\pi^0$  and  $\pi^+$  on the proton. Most of these experiments did not use polarization degrees of freedom, except for the longitudinal and transverse polarizations of the virtual photon in electroproduction,

which are accessible in experiments with large (azimuthal) angular coverage. However, especially in the  $\Delta(1232)$  region, some experiments were performed also with polarized electrons and polarized targets. In Hall A, Kelly et al. [30] even performed an almost complete experiment, which yielded 16 unpolarized and recoil polarization observables at  $Q^2 = 1.0 \text{ GeV}^2$ .

In parallel with the ongoing experiments, several theoretical groups developed models and analysis techniques, which were applied to the data. The model-independent GWU/SAID analysis [35,36] mostly analyzed the pion photoproduction data and improved the values of the photon couplings over the years. In addition, this group analyzed also the  $N\Delta$  transition form factors [37]. However, the model-independent ansatz used in the SAID analysis could not determine the  $Q^2$  dependence of the transition form factors in a reliable way because of rather limited experimental input from polarization observables. Further coupled channels analyses were performed by the Giessen group [38,39] and by the Bonn-Gatchina group [40,41]. Transition amplitudes were also determined in the framework of dynamically generated resonances by coupling to meson-baryon channels, e.g., for the  $S_{11}(1535)$  resonance by the Jülich group [42,43,44]. In addition, the nature of  $N^*$  resonances and their physical meaning was investigated within chiral effective field theory [45,46,47], and in particular the  $\Delta(1232)$  magnetic form factor and the  $E/M$  ratio was evaluated by different approaches [48,49,50,51]. Furthermore, dynamical models as the Dubna-Mainz-Taipei (DMT) model [52,53] and the Sato-Lee model [54] as well as its extensions by the EBAC group [55,56] were used to analyze photo- and electroproduction in the framework of bare and dressed nucleon resonances. However, most successful concerning the general applicability to the higher resonances, were the unitary isobar models of the Mainz group (MAID model) [57,58,59,60,61] and of the JLab group [62,63,64] who used dispersion relations as an additional constraint to reduce the model dependence due to incomplete experimental input.

With our unitary isobar model MAID, we analyzed all available electroproduction data in order to determine the transition form factors for all four-star resonances below  $W = 1.8 \text{ GeV}$ . In most cases we could obtain both single- $Q^2$  and  $Q^2$ -dependent transition form factors for the proton target. In the case of the neutron, the parametrization of the  $Q^2$  dependence had to take a simpler form because of the much smaller world database. Already in 2003 [59] we obtained transverse transition form factors for the  $\Delta(1232)$ ,  $P_{11}(1440)$ ,  $S_{11}(1535)$ ,  $D_{13}(1520)$ , and  $F_{15}(1680)$  as well as longitudinal form factors for the  $\Delta(1232)$ ,  $P_{11}(1440)$ , and  $S_{11}(1535)$  by using unpolarized  $\pi^0$  electroproduction data in the range of  $Q^2 = 0.4 - 1.5 \text{ GeV}^2$  [27,26].

The main motivation for exploring the nucleon transition form factors is to obtain a precise knowledge of the nucleon excitation spectrum, which provides — together with the elastic form factors — a complete description of the nucleon's electromagnetic structure. This structure can be compared with QCD inspired quark models and, in recent years, more and more also with lattice QCD calculations [65,66,67,68]. Moreover, the nucleon transition form factors provide an essential input for dispersive calculations of both sum rules and two-photon corrections to electron scattering [69,70,71,72,73].

Finally, the precise e.m. FF data yield the information to map out the quark charge densities in a baryon. A proper interpretation of such densities was found by looking at the baryon in the light-front frame. This procedure yields the spatial distribution of the quark charges in the plane transverse to the line-of-sight. Along these lines, the transverse charge densities of the quarks were mapped out for both the nucleon [74,75] and the deuteron [76] on the basis of empirical FF data. If precise transition FF data are available, the same technique can also be applied to map out the transition densities for nucleon resonance excitation. The resulting density plots reveal the spatial distribution of the quark charges inducing the excitation of a

particular resonance and provide an immediate view at its multipole structure. Using the empirical information on the  $N \rightarrow N^*$  transition form factors from the MAID analysis [58], the transition charge densities were mapped out for the transitions  $N \rightarrow \Delta(1232)$  [75] and  $N \rightarrow P_{11}(1440)$  [89]. Most recently we have extended this method to the quark transition charge densities inducing the e.m. excitations of the  $S_{11}(1535)$  and  $D_{13}(1520)$  resonances [61].

## 2 Electromagnetic couplings and transition form factors

The transverse photon couplings  $A_{1/2}$  and  $A_{3/2}$  listed by the PDG are related to the helicity amplitudes of pion photoproduction,  $A_{\ell\pm}$  and  $B_{\ell\pm}$ , as follows [77]:

$$A_{\ell\pm} = \mp \alpha C_{\pi N} A_{1/2}, \quad (9)$$

$$B_{\ell\pm} = \mp \frac{4\alpha}{\sqrt{(2J-1)(2J+3)}} C_{\pi N} A_{3/2}, \quad (10)$$

where

$$\alpha \equiv \sqrt{\frac{1}{\pi} \frac{k}{q} \frac{1}{(2J+1)} \frac{M_N}{M_R} \frac{\Gamma_\pi}{\Gamma^2}}. \quad (11)$$

Here  $k$  and  $q$  are the photon and pion c.m. momenta at  $W = M_R$ ,  $J$  is the angular momentum,  $M_R$  the mass,  $\Gamma$  the full width, and  $\Gamma_\pi$  the  $N\pi$  partial width of the resonance. Furthermore,  $M_N$  is the nucleon mass and  $C_{\pi N}$  is the Clebsch Gordan coefficient for the decay of the resonance into the relevant  $N\pi$  charge state. This coefficient is  $\sqrt{3/2}$  for isospin  $I = 3/2$  and  $-1/\sqrt{3}$  for  $I = 1/2$ . The helicity amplitudes are related to the usual electric and magnetic multipoles by

$$A_{\ell+} = \frac{1}{2} [(\ell+2)E_{\ell+} + \ell M_{\ell+}], \quad (12)$$

$$B_{\ell+} = E_{\ell+} - M_{\ell+}, \quad (13)$$

$$A_{\ell+1,-} = \frac{1}{2} [(\ell+2)M_{\ell+1,-} - \ell E_{\ell+1,-}], \quad (14)$$

$$B_{\ell+1,-} = E_{\ell+1,-} + M_{\ell+1,-}. \quad (15)$$

The  $N\gamma$  partial width  $\Gamma_\gamma$  is then given by

$$\Gamma_\gamma = \frac{k^2}{\pi} \frac{2M_N}{(2J+1)M_R} [|A_{1/2}|^2 + |A_{3/2}|^2]. \quad (16)$$

However, this formulation as explicitly given, e.g., in PDG(1992) [77], needs some additional interpretation. In order to obtain a pure resonance coupling, the pion photoproduction amplitudes must be separated in resonance and background parts. This separation is in general a model-dependent issue. Mathematically, the cleanest way is to separate the amplitudes at the pole position and to identify the resonance part by the residues in each helicity channel. The first steps to study the e.m.  $\Delta(1232)$  excitation at the pole position were made by Hanstein et al. [23] and Workman et al. [78]. Very recently also the Bonn-Gatchina [41] and the EBAC [56] groups have started to derive the photon couplings for higher resonances at the  $t$ -matrix pole. Of course, the pole values arising from complex residues will eventually lead to complex photon couplings and complex form factors.

Here and in most publications as well as in all the listings of PDG, the resonance-background separation has been performed in a Breit-Wigner formalism. A typical ansatz can be found in an early publication of the SAID group [35].

Starting from the photon couplings, the transverse transition form factors in the helicity basis can be straightforwardly introduced by defining the functions  $A_{1/2}(Q^2)$  and  $A_{3/2}(Q^2)$ . The FFs of the transverse e.m. multipoles follow from the above equations in an analogous way. In addition, a third form factor  $S_{1/2}(Q^2)$  appears due to the longitudinal photon field in the same partial wave. The details and conventions used will be given in the next section where we describe our MAID ansatz for obtaining the form factors.

### 3 The MAID ansatz

In the spirit of a dynamical approach to pion photo- and electroproduction, the  $t$ -matrix of the unitary isobar model is set up by the ansatz

$$t_{\gamma\pi}(W) = t_{\gamma\pi}^B(W) + t_{\gamma\pi}^R(W), \quad (17)$$

with a background and a resonance  $t$ -matrix, each of them constructed in a unitary way. Of course, this ansatz is not unique. However, it is a very important prerequisite to clearly separate resonance and background amplitudes within a Breit-Wigner concept also for higher and overlapping resonances.

For a specific partial wave  $\alpha = \{j, l, \dots\}$ , the background  $t$ -matrix is set up by a potential multiplied by the pion-nucleon scattering amplitude in accordance with the K-matrix approximation,

$$t_{\gamma\pi}^{B,\alpha}(W, Q^2) = v_{\gamma\pi}^{B,\alpha}(W, Q^2) [1 + it_{\pi N}^\alpha(W)], \quad (18)$$

where only the on-shell part of pion-nucleon rescattering is maintained and the off-shell part from pion-loop contributions is neglected. Whereas this approximation would fail near the threshold for  $\gamma, \pi^0$  [79,80], it is well justified in the resonance region because the main contribution from pion-loop effects is absorbed by the nucleon resonance dressing.

The background potential  $v_{\gamma\pi}^{B,\alpha}(W, Q^2)$  is described by Born terms obtained with an energy-dependent mixing of pseudovector-pseudoscalar  $\pi NN$  coupling and  $t$ -channel vector meson exchanges. The mixing parameters and coupling constants are determined by an analysis of nonresonant multipoles in the appropriate energy regions [57]. In the latest version MAID2007 [58], the  $S$ ,  $P$ ,  $D$ , and  $F$  waves of the background contributions are unitarized as explained above, with the pion-nucleon elastic scattering amplitudes,  $t_{\pi N}^\alpha = [\eta_\alpha \exp(2i\delta_\alpha) - 1]/2i$ , described by phase shifts  $\delta_\alpha$  and the inelasticity parameters  $\eta_\alpha$  taken from the GWU/SAID analysis [36].

For the resonance contributions we follow Ref. [57] and assume Breit-Wigner forms for the resonance shape,

$$t_{\gamma\pi}^{R,\alpha}(W, Q^2) = \bar{\mathcal{A}}_\alpha^R(W, Q^2) \frac{f_{\gamma N}(W) \Gamma_{tot}(W) M_R f_{\pi N}(W)}{M_R^2 - W^2 - i M_R \Gamma_{tot}(W)} e^{i\phi_R(W, Q^2)}, \quad (19)$$

where  $f_{\pi N}(W)$  is the usual Breit-Wigner factor describing the decay of a resonance with total width  $\Gamma_{tot}(W)$ , partial  $\pi N$  width  $\Gamma_{\pi N}(W)$ , and spin  $j$ ,

$$f_{\pi N}(W) = C_{\pi N} \left[ \frac{1}{(2j+1)\pi} \frac{\kappa(W)}{q(W)} \frac{M_N}{M_R} \frac{\Gamma_{\pi N}(W)}{\Gamma_{tot}^2(W)} \right]^{1/2}, \quad (20)$$

with

$$k(W, Q^2) = \frac{\sqrt{(Q^2 + (W + M_N)^2)(Q^2 + (W - M_N)^2)}}{2W}, \quad (21)$$

$$q(W) = \frac{\sqrt{(W^2 - (M_N + m_\pi)^2)(W^2 - (M_N - m_\pi)^2)}}{2W}, \quad (22)$$

$$\kappa(W) = \frac{W^2 - M_N^2}{2W}, \quad (23)$$

and  $C_{\pi N} = \sqrt{3/2}$  and  $-1/\sqrt{3}$  for isospin  $\frac{3}{2}$  and  $\frac{1}{2}$ , respectively. The energy dependence of the partial width is given by

$$\Gamma_{\pi N}(W) = \beta_\pi \Gamma_R \left( \frac{q(W)}{q_R} \right)^{2l+1} \left( \frac{X_R^2 + q_R^2}{X_R^2 + q^2(W)} \right)^\ell \frac{M_R}{W}, \quad (24)$$

with  $q_R = q(M_R)$ ,  $\Gamma_R = \Gamma_{\text{tot}}(M_R)$ ,  $X_R$  a damping parameter (cut-off), and  $\beta_\pi$  the single-pion branching ratio. The expression for the total width  $\Gamma_{\text{tot}}$  is given in Ref. [57]. The  $\gamma NN^*$  vertex is assumed to have the following dependence on  $W$ :

$$f_{\gamma N}(W) = \left( \frac{\kappa(W)}{\kappa_R} \right)^n \left( \frac{X_R^2 + \kappa_R^2}{X_R^2 + \kappa^2(W)} \right), \quad (25)$$

where  $\kappa_R = \kappa(M_R)$  and  $n$  is obtained from a best fit to the real photon data. The phase  $\phi_R(W, Q^2)$  in Eq. (19) is introduced to adjust the total phase such that the Fermi-Watson theorem is fulfilled below two-pion threshold. For the  $S$ - and  $P$ -wave multipoles we extend this unitarization procedure up to  $W = 1400$  MeV. Because of a lack of further information, we assume that the phases  $\phi_R$  are constant at the higher energies. In particular we note that the phase  $\phi_R$  for the  $P_{33}(1232)$  excitation vanishes at  $W = M_R = 1232$  MeV for all values of  $Q^2$ . For this multipole we may even apply the Fermi-Watson theorem up to  $W \approx 1600$  MeV because the inelasticity parameter  $\eta_\alpha$  remains close to 1. For the  $D$ - and  $F$ -wave resonances, the phases  $\phi_R$  are set to be constant and determined from the best fit.

**Table 1.** The reduced e.m. amplitudes  $\bar{\mathcal{A}}_\alpha$  defined by Eq. (19) in terms of the helicity amplitudes.

$N^*$	$E$	$M$	$S$
$S_{11}/S_{31}$	$-A_{1/2}$	—	$-\sqrt{2}S_{1/2}$
$P_{13}/P_{33}$	$\frac{1}{2}(\frac{1}{\sqrt{3}}A_{3/2} - A_{1/2})$	$-\frac{1}{2}(\sqrt{3}A_{3/2} + A_{1/2})$	$-\frac{1}{\sqrt{2}}S_{1/2}$
$P_{11}/P_{31}$	—	$A_{1/2}$	$-\sqrt{2}S_{1/2}$
$D_{13}/D_{33}$	$-\frac{1}{2}(\sqrt{3}A_{3/2} + A_{1/2})$	$-\frac{1}{2}(\frac{1}{\sqrt{3}}A_{3/2} - A_{1/2})$	$-\frac{1}{\sqrt{2}}S_{1/2}$
$D_{15}/D_{35}$	$\frac{1}{3}(\frac{1}{\sqrt{2}}A_{3/2} - A_{1/2})$	$-\frac{1}{3}(\sqrt{2}A_{3/2} + A_{1/2})$	$-\frac{\sqrt{2}}{3}S_{1/2}$
$F_{15}/F_{35}$	$-\frac{1}{3}(\sqrt{2}A_{3/2} + A_{1/2})$	$-\frac{1}{3}(\frac{1}{\sqrt{2}}A_{3/2} - A_{1/2})$	$-\frac{\sqrt{2}}{3}S_{1/2}$
$F_{17}/F_{37}$	$\frac{1}{4}(\sqrt{\frac{3}{5}}A_{3/2} - A_{1/2})$	$-\frac{1}{4}(\sqrt{\frac{5}{3}}A_{3/2} + A_{1/2})$	$-\frac{1}{2\sqrt{2}}S_{1/2}$

The more commonly used helicity amplitudes  $A_{1/2}$ ,  $A_{3/2}$ , and  $S_{1/2}$  are given by linear combinations of the e.m. couplings  $\bar{\mathcal{A}}_\alpha^R$ . These relations take the form

$$A_{1/2}^{\ell+} = -\frac{1}{2}[(\ell+2)\bar{E}_{\ell+} + \ell\bar{M}_{\ell+}], \quad (26)$$

$$A_{3/2}^{\ell+} = \frac{1}{2}\sqrt{\ell(\ell+2)}(\bar{E}_{\ell+} - \bar{M}_{\ell+}), \quad (27)$$

$$S_{1/2}^{\ell+} = -\frac{\ell+1}{\sqrt{2}}\bar{S}_{\ell+} \quad (28)$$



for resonances with total spin  $j = \ell + \frac{1}{2}$ , and

$$A_{1/2}^{\ell-} = \frac{1}{2}[(\ell + 1)\bar{M}_{\ell-} - (\ell - 1)\bar{E}_{\ell-}], \quad (29)$$

$$A_{3/2}^{\ell-} = -\frac{1}{2}\sqrt{(\ell - 1)(\ell + 1)}(\bar{E}_{\ell-} + \bar{M}_{\ell-}), \quad (30)$$

$$S_{1/2}^{\ell-} = -\frac{\ell}{\sqrt{2}}\bar{S}_{\ell-} \quad (31)$$

for resonances with total spin  $j = \ell - \frac{1}{2}$ . The inverse relations for the partial waves are listed in Table 1. The helicity amplitudes are related to matrix elements of the e.m. current  $J_\mu$  between the nucleon and the resonance states, e.g., as obtained in the framework of quark models,

$$A_{1/2} = -\sqrt{\frac{2\pi\alpha_{\text{em}}}{\kappa_R}} \langle N^*, \frac{1}{2} | J_+ | N, -\frac{1}{2} \rangle \zeta, \quad (32)$$

$$A_{3/2} = -\sqrt{\frac{2\pi\alpha_{\text{em}}}{\kappa_R}} \langle N^*, \frac{3}{2} | J_+ | N, \frac{1}{2} \rangle \zeta, \quad (33)$$

$$S_{1/2} = +\sqrt{\frac{2\pi\alpha_{\text{em}}}{\kappa_R}} \langle N^*, \frac{1}{2} | \rho | N, \frac{1}{2} \rangle \zeta, \quad (34)$$

where  $J_+ = -\frac{1}{\sqrt{2}}(J_x + iJ_y)$  and  $\alpha_{\text{em}} = 1/137$ . However, these equations define the couplings only up to a phase  $\zeta$ , which in principle can be obtained from the pionic decay of the resonance calculated within the same model. Because this phase is often ignored in the literature, the comparison of the sign is not always meaningful, especially in critical cases such as the Roper resonance for which the correct sign is not obvious from the data. MAID uses the helicity amplitudes  $A_{1/2}$ ,  $A_{3/2}$ , and  $S_{1/2}$  for photoproduction as input parameters, except for the  $P_{33}(1232)$  resonance which is directly described by the three e.m. amplitudes  $\bar{A}_\alpha$ .

While the original version of MAID included only the 7 most important nucleon resonances with only transverse e.m. couplings in most cases, MAID2007 describes all 13 four-star resonances below  $W = 2$  GeV:  $P_{33}(1232)$ ,  $P_{11}(1440)$ ,  $D_{13}(1520)$ ,  $S_{11}(1535)$ ,  $S_{31}(1620)$ ,  $S_{11}(1650)$ ,  $D_{15}(1675)$ ,  $F_{15}(1680)$ ,  $D_{33}(1700)$ ,  $P_{13}(1720)$ ,  $F_{35}(1905)$ ,  $P_{31}(1910)$ , and  $F_{37}(1950)$ .

In Tables 3 and 4 we compare the helicity amplitudes obtained from MAID2007 with the results of the PDG [1], GWU/SAID [81,82], Bonn-Gatchina [41], and Giessen [38,39] analyses. As is very typical for a global analysis with about 20,000 data points fitted to a small set of 20-30 parameters, the fit errors appear unrealistically small. However, one should realize that these errors only reflect the statistical uncertainty of the experimental error, whereas the model uncertainty can be larger by an order of magnitude. We therefore do not list our fit errors, which in fact are very similar to the fits of the SAID group [82,81]. The only realistic error estimate is obtained by comparing different analyses, such as SAID, MAID, and coupled-channels approaches. A comparison between the analyses of the different groups with different models and methods, listed in Table 3, shows a rather clear hierarchy among the resonances that all have an overall four-star ranking (see also Fig. 1). The most reliable e.m. couplings are known from  $P_{33}$ ,  $D_{13}$  and  $F_{15}$ , whereas even from the latter two only the large  $A_{3/2}$  amplitudes show this quality. The  $P_{11}$ ,  $S_{11}$  and  $F_{37}$  are reasonably well known but for the  $D_{15}$ ,  $D_{33}$  and  $F_{35}$  the couplings show already a larger spread. Badly known and unreliable are the couplings for the second  $S_{11}$ , the  $S_{31}$ ,  $P_{13}$  and  $P_{31}$ . Electromagnetic resonance couplings for states with overall status of less than four-star should rather be considered as unknown. In most present analyses and models these states are

**Table 2.** Masses, widths, single-pion branching ratios, and angles  $\phi_R$  included in the MAID analysis. Masses and widths are given in MeV, angles in degrees, the branching ratios  $\beta_\pi$  and  $\beta_\gamma$  in %. The quoted PDG ranges are from Ref. [1].

$N^*, \Delta$	$M_{R,PDG}$	$\Gamma_{R,PDG}$	$\beta_{\pi,PDG}$	$\beta_{\gamma,PDG}^p$	$M_R$	$\Gamma_R$	$\beta_\pi$	$\phi_R$
$P_{33}(1232)$	1231-1233	116-120	100	0.52-0.60	1232	130	100	0.0
$P_{11}(1440)$	1420-1470	200-450	55-75	0.035-0.048	1440	350	70	-15
$D_{13}(1520)$	1515-1525	100-125	55-65	0.46-0.56	1530	130	60	32
$S_{11}(1535)$	1525-1545	125-175	35-55	0.15-0.35	1535	100	40	8.2
$P_{33}(1600)$	1550-1700	250-460	10-25	0.001-0.020				
$S_{31}(1620)$	1600-1660	135-150	20-30	0.004-0.044	1620	150	25	23
$S_{11}(1650)$	1645-1670	145-185	60-95	0.04-0.18	1690	100	85	7.0
$D_{15}(1675)$	1670-1680	130-165	35-45	0.004-0.023	1675	150	45	20
$F_{15}(1680)$	1680-1690	120-140	65-70	0.21-0.32	1680	135	70	10
$D_{13}(1700)$	1650-1750	050-150	05-15	0.01-0.05				
$P_{11}(1710)$	1680-1690	120-140	65-70	0.002-0.050				
$D_{33}(1700)$	1670-1750	200-400	10-20	0.12-0.26	1740	450	15	61
$P_{13}(1720)$	1700-1750	150-300	10-20	0.003-0.100	1740	250	20	0.0
$F_{35}(1905)$	1865-1915	270-400	09-15	0.01-0.03	1905	350	10	40
$P_{31}(1910)$	1870-1920	190-270	15-30	0.0-0.2	1910	250	25	35
$P_{33}(1920)$	1900-1970	150-300	05-20					
$D_{35}(1930)$	1900-2020	220-500	05-15	0.00-0.02				
$F_{37}(1950)$	1915-1950	235-335	35-45	0.08-0.13	1945	280	40	30

neglected. However, with the advent of ‘complete experiments’ and the analysis of double-polarization observables a big improvement in this field is already in sight.

## 4 Transition form factors

In most cases, the resonance couplings  $\bar{\mathcal{A}}_\alpha^R(W, Q^2)$  are assumed to be independent of the total energy. However, an energy dependence may occur if the resonance is parameterized in terms of the virtual photon three-momentum  $k(W, Q^2)$ , e.g., in MAID2007 for the  $\Delta(1232)$  resonance. For all other resonances discussed here, we may assume a simple  $Q^2$  dependence,  $\bar{\mathcal{A}}_\alpha(Q^2)$ . These resonance couplings are taken as constants for a single- $Q^2$  analysis, e.g., for photoproduction ( $Q^2 = 0$ ) but also at any fixed  $Q^2 > 0$ , whenever sufficient data with  $W$  and  $\theta$  variation are available, see Table 5. Alternatively the couplings can be parameterized as functions of  $Q^2$  by an ansatz like

$$\bar{\mathcal{A}}_\alpha(Q^2) = \bar{\mathcal{A}}_\alpha(0)(1 + a_1Q^2 + a_2Q^4 + a_3Q^6 + a_4Q^8) e^{-b_1Q^2}. \quad (35)$$

For such an ansatz the parameters  $\bar{\mathcal{A}}_\alpha(0)$  are determined by a fit to the world database of photoproduction, and the parameters  $a_i$  and  $b_1$  are obtained from a combined fitting of all the electroproduction data at different  $Q^2$ . The latter procedure is called the  $Q^2$ -dependent fit. In MAID the photon couplings  $\bar{\mathcal{A}}_\alpha(0)$  are input parameters, directly related to the helicity couplings  $A_{1/2}$ ,  $A_{3/2}$ , and  $S_{1/2}$  of nucleon resonance excitation. For further details see Ref. [58].

In Tables 6, 7, and 8 we list the parameters obtained from our new  $Q^2$ -dependent fit to the resonances above the  $\Delta(1232)$ . Because we have recently included the 2008  $\pi^+$  data of Park et al. [33] in our database, our new results differ from the MAID2007 parametrization for the following six proton transition form factors:  $P_{11}(1440)$ ,

**Table 3.** Proton helicity amplitudes at  $Q^2 = 0$  for the major nucleon resonances, in units  $10^{-3} \text{ GeV}^{-1/2}$ . The results with MAID(MD07) [58] are compared to the PDG [1], GWU/SAID(SP09) [81], Bonn-Gatchina [41], and Gießen (GI02/07) [38,39] analysis.

<sup>1</sup> In the SP09 analysis, the  $\pi N$  branching ratio for the  $S_{11}(1650)$  is 100%.

		PDG	SP09	BoGa09	GI02/07	MD07
$P_{33}(1232)$	$A_{1/2}$	$-135 \pm 6$	$-139.6 \pm 1.8$	$-136 \pm 5$	-128	-140
	$A_{3/2}$	$-250 \pm 8$	$-258.9 \pm 2.3$	$-267 \pm 8$	-247	-265
$P_{11}(1440)$	$A_{1/2}$	$-65 \pm 4$	$-56.4 \pm 1.7$	$-52 \pm 10$	-84	-61
$D_{13}(1520)$	$A_{1/2}$	$-24 \pm 9$	$-26.0 \pm 1.5$	$-32 \pm 6$	-15	-27
	$A_{3/2}$	$166 \pm 5$	$141.2 \pm 1.7$	$138 \pm 8$	146	161
$S_{11}(1535)$	$A_{1/2}$	$90 \pm 30$	$100.9 \pm 3.0$	$90 \pm 15$	95	66
$S_{31}(1620)$	$A_{1/2}$	$27 \pm 11$	$47.2 \pm 2.3$	$63 \pm 12$	-50	66
$S_{11}(1650)$	$A_{1/2}$	$53 \pm 16$	$9.0 \pm 9.1^1$	$60 \pm 20$	57	33
$D_{15}(1675)$	$A_{1/2}$	$19 \pm 8$	$14.9 \pm 2.1$	$21 \pm 4$	9	15
	$A_{3/2}$	$15 \pm 9$	$18.4 \pm 2.1$	$24 \pm 8$	21	22
$F_{15}(1680)$	$A_{1/2}$	$-15 \pm 6$	$-17.6 \pm 1.5$	$-12 \pm 6$	3	-25
	$A_{3/2}$	$133 \pm 12$	$134.2 \pm 1.6$	$136 \pm 12$	116	134
$D_{33}(1700)$	$A_{1/2}$	$104 \pm 15$	$118.3 \pm 3.3$	$160 \pm 45$	96	226
	$A_{3/2}$	$85 \pm 22$	$110.0 \pm 3.5$	$160 \pm 40$	154	210
$P_{13}(1720)$	$A_{1/2}$	$18 \pm 30$	$90.5 \pm 3.3$	$130 \pm 50$	-65	73
	$A_{3/2}$	$-19 \pm 20$	$-36.0 \pm 3.9$	$100 \pm 50$	35	-11
$F_{35}(1905)$	$A_{1/2}$	$26 \pm 11$	$11.4 \pm 8.0$	$28 \pm 12$		18
	$A_{3/2}$	$-45 \pm 20$	$-51.0 \pm 8.0$	$-42 \pm 15$		-28
$P_{31}(1910)$	$A_{1/2}$	$3 \pm 14$				18
$F_{37}(1950)$	$A_{1/2}$	$-76 \pm 12$	$-71.5 \pm 1.8$	$-83 \pm 8$		-94
	$A_{3/2}$	$-97 \pm 10$	$-94.7 \pm 1.8$	$-92 \pm 8$		-121

**Table 4.** Neutron helicity amplitudes at  $Q^2 = 0$  for the major nucleon resonances, in units  $10^{-3} \text{ GeV}^{-1/2}$ . The results with MAID(MD07) [58] are compared to the PDG [1], GWU/SAID(GW02) [82] and Gießen(GI07) [39] analysis.

		PDG	GW02	GI02/07	MD07
$P_{11}(1440)$	$A_{1/2}$	$40 \pm 10$	$47 \pm 5$	138	54
$D_{13}(1520)$	$A_{1/2}$	$-59 \pm 9$	$-67 \pm 4$	-64	-77
	$A_{3/2}$	$-139 \pm 11$	$-112 \pm 3$	-136	-154
$S_{11}(1535)$	$A_{1/2}$	$-46 \pm 27$	$-16 \pm 5$	-74	-51
$S_{11}(1650)$	$A_{1/2}$	$-15 \pm 21$	$-28 \pm 4$	-9	9
$D_{15}(1675)$	$A_{1/2}$	$-43 \pm 12$	$-50 \pm 4$	-56	-62
	$A_{3/2}$	$-58 \pm 13$	$-71 \pm 5$	-84	-84
$F_{15}(1680)$	$A_{1/2}$	$29 \pm 10$	$29 \pm 6$	30	28
	$A_{3/2}$	$-33 \pm 9$	$-58 \pm 9$	-48	-38
$P_{13}(1720)$	$A_{1/2}$	$1 \pm 15$		3	-3
	$A_{3/2}$	$-29 \pm 61$		-1	-31

$D_{13}(1520)$ ,  $D_{33}(1700)$ ,  $D_{15}(1675)$ ,  $F_{15}(1680)$ , and  $P_{13}(1720)$ . Our parametrization of the  $\Delta(1232)$  form factors is more complicated, in particular due to built-in requirements from low-energy theorems in the Siegert limit, as discussed in Ref. [58] in further details.

Above the third resonance region there is an energy gap between 1800–1900 MeV where no four-star resonances have been found. Beyond this gap and up to 2 GeV,

**Table 5.** Database of pion electroproduction for energies above the  $\Delta$  resonance up to  $W = 1.7$  GeV, which is used in our single- $Q^2$  transition form factor analysis.

Reference	year	reaction	$Q^2$ ( $GeV^2$ )
Frolov et al.[25]	1999	$p\pi^0$	2.8 – 4.0
Gothe et al.[16]	2000	$p\pi^0$	0.63
Pospischil et al.[13]	2001	$p\pi^0$	0.121
Mertz et al.[18]	2001	$p\pi^0$	0.126
Joo et al.[27]	2002	$p\pi^0$	0.4 – 1.8
Joo et al.[29]	2004	$n\pi^+$	0.4 – 0.65
Laveissiere et al.[26]	2004	$p\pi^0$	1.0
Kelly et al.[30]	2005	$p\pi^0$	1.0
Elsner et al.[14]	2006	$p\pi^0$	0.20
Stave et al.[15]	2006	$p\pi^0$	0.06
Egiyan et al.[31]	2006	$n\pi^+$	0.3 – 0.6
Ungaro et al.[32]	2006	$p\pi^0$	3.0 – 6.0
Park et al.[33]	2008	$n\pi^+$	1.7 – 4.5
Villano et al.[34]	2009	$p\pi^0$	6.4 – 7.7

**Table 6.** New MAID2008 parametrization of the transition form factors, Eq. (35), for proton targets.  $\bar{A}_\alpha(0)$  is given in units of  $10^{-3} GeV^{-1/2}$  and the coefficients  $a_1, a_2, a_4, b_1$  in units of  $GeV^{-2}, GeV^{-4}, GeV^{-8}, GeV^{-2}$ , respectively. For all fits  $a_3 = 0$ .

$N^*, \Delta^*$		$\bar{A}_\alpha(0)$	$a_1$	$a_2$	$a_4$	$b_1$
$P_{11}(1440)p$	$A_{1/2}$	-61.4	0.871	-3.516	-0.158	1.36
	$S_{1/2}$	4.2	40.	0	1.50	1.75
$D_{13}(1520)p$	$A_{1/2}$	-27.4	8.580	-0.252	0.357	1.20
	$A_{3/2}$	160.6	-0.820	0.541	-0.016	1.06
$D_{15}(1675)p$	$S_{1/2}$	-63.5	4.19	0	0	3.40
	$A_{1/2}$	15.3	0.10	0	0	2.00
$F_{15}(1680)p$	$A_{3/2}$	21.6	1.91	0.18	0	0.69
	$S_{1/2}$	1.1	0	0	0	2.00
$F_{15}(1680)p$	$A_{1/2}$	-25.1	3.780	-0.292	0.080	1.25
	$A_{3/2}$	134.3	1.016	0.222	0.237	2.41
$D_{33}(1700)$	$S_{1/2}$	-44.0	3.783	0	0	1.85
	$A_{1/2}$	226.	1.91	0	0	1.77
$P_{13}(1720)p$	$A_{3/2}$	210.	0.88	1.71	0	2.02
	$S_{1/2}$	2.1	0	0	0	2.00
$P_{13}(1720)p$	$A_{1/2}$	73.0	1.89	0	0	1.55
	$A_{3/2}$	-11.5	10.83	-0.66	0	0.43
	$S_{1/2}$	-53.0	2.46	0	0	1.55

three more four-star resonances are listed in PDG,  $F_{35}(1905), P_{31}(1910)$ , and  $F_{37}(1950)$ , which are also included in MAID. There is essentially nothing known about these states in electroproduction, and we have just introduced their reported photon couplings, multiplied with a simple gaussian form factor,  $\exp(-2.0 Q^2/GeV^2)$ . The main role of these resonances in MAID is to define a global high-energy behavior that is needed for applications with dispersion relations and sum rules. Future experiments in this region will give us the necessary information to map out these form factors in more detail.

**Table 7.** Maid2007 parameterizations, Eq. (35), for proton targets ( $a_{2,3,4} = 0$ ).

$N^*, \Delta^*$		$\mathcal{A}_\alpha(0)$	$a_1$	$b_1$
$S_{11}(1535)p$	$A_{1/2}$	66.4	1.608	0.70
	$S_{1/2}$	-2.0	23.9	0.81
$S_{31}(1620)$	$A_{1/2}$	65.6	1.86	2.50
	$S_{1/2}$	16.2	2.83	2.00
$S_{11}(1650)p$	$A_{1/2}$	33.3	1.45	0.62
	$S_{1/2}$	-3.5	2.88	0.76

**Table 8.** Same as Table 7, for neutron targets.

$N^*$		$\mathcal{A}_\alpha(0)$	$a_1$	$b_1$
$P_{11}(1440)n$	$A_{1/2}$	54.1	0.95	1.77
	$S_{1/2}$	-41.5	2.98	1.55
$D_{13}(1520)n$	$A_{1/2}$	-76.5	-0.53	1.55
	$A_{3/2}$	-154.	0.58	1.75
	$S_{1/2}$	13.6	15.7	1.57
$S_{11}(1535)n$	$A_{1/2}$	-50.7	4.75	1.69
	$S_{1/2}$	28.5	0.36	1.55
$S_{11}(1650)n$	$A_{1/2}$	9.3	0.13	1.55
	$S_{1/2}$	10.	-0.50	1.55
$D_{15}(1675)n$	$A_{1/2}$	-61.7	0.01	2.00
	$A_{3/2}$	-83.7	0.01	2.00
	$S_{1/2}$	0	0	0
$F_{15}(1680)n$	$A_{1/2}$	27.9	0	1.20
	$A_{3/2}$	-38.4	4.09	1.75
	$S_{1/2}$	0	0	0
$P_{13}(1720)n$	$A_{1/2}$	-2.9	12.70	1.55
	$A_{3/2}$	-31.0	5.00	1.55
	$S_{1/2}$	0	0	0

#### 4.1 First Resonance Region

The  $\Delta(1232)P_{33}$  is the only nucleon resonance with a well-defined Breit-Wigner resonance position,  $M_R = 1232$  MeV. It is an ideal single-channel resonance, the Watson theorem applies, and the Breit-Wigner position coincides with the K-matrix pole position. For these reasons, the  $N \rightarrow \Delta(1232)$  form factors can be determined in an essentially model independent way.

The magnetic form factor shown in Fig. 5 is very well known up to high momentum transfer,  $Q^2 = 10$  GeV<sup>2</sup>, and can be parameterized in a surprisingly simple form found in our previous MAID analysis,

$$G_M^*(Q^2) = 3 G_D(Q^2) e^{-0.21Q^2/\text{GeV}^2}, \quad (36)$$

with  $G_D$  the standard dipole form factor. The electric and Coulomb form factors are much smaller and are usually given as ratios to the magnetic form factor.

In the literature the e.m. properties of the  $N\Delta(1232)$  transition are described by either the magnetic ( $G_M^*$ ), electric ( $G_E^*$ ), and Coulomb ( $G_C^*$ ) form factors or the helicity amplitudes  $A_{1/2}$ ,  $A_{3/2}$ , and  $S_{1/2}$ , which can be derived from the reduced e.m. amplitudes  $\mathcal{A}_\alpha$  defined by Eq. (19). It is worthwhile pointing out that the latter amplitudes are related to the multipoles over the full energy region, that is, they are the primary target of the fitting procedure. The form factors and helicity amplitudes

are then obtained by evaluating the reduced e.m. amplitudes at the resonance position  $W = M_\Delta = 1232$  MeV. The respective relations take the form

$$G_M^*(Q^2) = -c_\Delta(A_{1/2} + \sqrt{3}A_{3/2}) = 2c_\Delta \bar{\mathcal{A}}_M^\Delta(M_\Delta, Q^2), \quad (37)$$

$$G_E^*(Q^2) = c_\Delta(A_{1/2} - \frac{1}{\sqrt{3}}A_{3/2}) = -2c_\Delta \bar{\mathcal{A}}_E^\Delta(M_\Delta, Q^2), \quad (38)$$

$$G_C^*(Q^2) = \sqrt{2}c_\Delta \frac{2M_\Delta}{k_\Delta} S_{1/2} = -2c_\Delta \frac{2M_\Delta}{k_\Delta} \bar{\mathcal{A}}_S^\Delta(M_\Delta, Q^2), \quad (39)$$

$$\text{with } c_\Delta = \left( \frac{M_N^3 \kappa_\Delta}{4\pi\alpha_{\text{em}} M_\Delta k_\Delta^2} \right)^{1/2}, \quad (40)$$

where  $k_\Delta = k_\Delta(Q^2) = k(M_\Delta, Q^2)$  and  $\kappa_\Delta = \kappa(M_\Delta) = k(M_\Delta, 0)$  are the virtual photon momentum and the photon equivalent energy at resonance. Because the  $\Delta(1232)$  is very close to an ideal resonance, the real parts of the amplitudes vanish at  $W = M_\Delta$ , and the form factors can be directly expressed by the imaginary parts of the corresponding multipoles at the resonance position,

$$G_M^*(Q^2) = b_\Delta \text{Im}\{M_{1+}^{(3/2)}(M_\Delta, Q^2)\}, \quad (41)$$

$$G_E^*(Q^2) = -b_\Delta \text{Im}\{E_{1+}^{(3/2)}(M_\Delta, Q^2)\}, \quad (42)$$

$$G_C^*(Q^2) = -b_\Delta \frac{2M_\Delta}{k_\Delta} \text{Im}\{S_{1+}^{(3/2)}(M_\Delta, Q^2)\}, \quad (43)$$

$$\text{where } b_\Delta = \left( \frac{8 M_N^2 q_\Delta \Gamma_\Delta}{3 \alpha_{\text{em}} k_\Delta^2} \right)^{1/2}, \quad (44)$$

and with  $\Gamma_\Delta = 115$  MeV and  $q_\Delta = q(M_\Delta)$  the pion momentum at resonance. The above definition of the form factors is due to Ash [5]. The form factors of Jones and Scadron [10] are obtained by multiplying our form factors with  $\sqrt{1 + Q^2/(M_N + M_\Delta)^2}$ . We note that the form factor  $G_C^*$  differs from our previous work [60] by the factor  $2M_\Delta/k_\Delta$  in Eq. (43). With these definitions all 3 transition form factors remain finite at pseudo-threshold (Siegert limit). In the literature, the following ratios of multipoles have been defined:

$$R_{EM} = \frac{E_{1+}^{3/2}}{M_{1+}^{3/2}} = -\frac{G_E^*}{G_M^*} = \frac{A_{1/2} - \frac{1}{\sqrt{3}}A_{3/2}}{A_{1/2} + \sqrt{3}A_{3/2}}, \quad (45)$$

$$R_{SM} = \frac{S_{1+}^{3/2}}{M_{1+}^{3/2}} = -\frac{k_\Delta}{2M_\Delta} \frac{G_C^*}{G_M^*} = \frac{\sqrt{2}S_{1/2}}{A_{1/2} + \sqrt{3}A_{3/2}}. \quad (46)$$

In MAID2007 the  $Q^2$  dependence of the e.m.  $N\Delta$  transition form factors is parameterized as follows:

$$G_{E,M}^*(Q^2) = g_{E,M}^0(1 + \beta_{E,M}Q^2)e^{-\gamma_{E,M}Q^2} G_D(Q^2), \quad (47)$$

$$G_C^*(Q^2) = g_C^0 \frac{1 + \beta_C Q^2}{1 + d_C Q^2/(4M_N^2)} \frac{2M_\Delta}{\kappa_\Delta} e^{-\gamma_C Q^2} G_D(Q^2), \quad (48)$$

where  $G_D(Q^2) = 1/(1 + Q^2/0.71 \text{ GeV}^2)^2$  is the dipole form factor. In order to fulfill the Siegert theorem, we have changed the parametrization of the Coulomb amplitude accordingly [58]. The result of MAID2007 for  $G_M^*(Q^2)$  is compared to the data in Fig. 5. Except for the latest data by Villano et al. [34] at the highest  $Q^2$  shown, our

**Table 9.** Parameters for the  $N\Delta$  transition form factors  $G_M^*$ ,  $G_E^*$ ,  $G_C^*$  given by Eqs. (47-48). The normalization values at the photon point ( $Q^2 = 0$ ),  $g_\alpha^0$  and  $d_\alpha$  are dimensionless, the parameters  $\beta$  and  $\gamma$  in  $\text{GeV}^{-2}$ .

	M1	E2	C2
$g_\alpha^0$	3.00	0.0637	0.1240
$\beta_\alpha$	0.0095	-0.0206	0.120
$\gamma_\alpha$	0.23	0.16	0.23
$d_\alpha$	0	0	4.9

single- $Q^2$  analysis for all other data follows the global fit closely and is not shown in the figure. We further note that  $G_M^*(0)/3$  takes the value of 1.0 to an accuracy of 1%. This value is related to the  $N \rightarrow \Delta$  magnetic transition moment,  $\mu_{N\Delta} = (3.46 \pm 0.03)$  nuclear magnetons, see Eq. (1), by the following equation:

$$G_M^*(0) = \sqrt{\frac{M_N}{M_\Delta}} \mu_{N\Delta}. \quad (49)$$

Figures 6 and 7 compare the MAID2007 solutions (solid lines) for the ratios  $R_{EM}$  and  $R_{SM}$  with other analyses. The ratio  $R_{EM}$  from MAID2007 stays always below the zero line, in agreement with the original analysis of the data [32,25] and also with the dynamical model of Sato and Lee [54] who concluded that  $R_{EM}$  remains negative and tends towards more negative values with increasing  $Q^2$ . This indicates that the predicted helicity conservation at the quark level is irrelevant for the present experimental  $Q^2$  range. We also analyzed the new data of Ref. [32] in the range of  $3 \text{ GeV}^2 \leq Q^2 \leq 6 \text{ GeV}^2$  and found slightly decreasing values of  $R_{EM}$  from our single- $Q^2$  analysis. For the ratio  $R_{SM}$  both the  $Q^2$ -dependent and the single- $Q^2$  fits approach a negative constant for large  $Q^2$ . This result is in good agreement with the prediction of Ji et al. [84] and of Buchmann [85] (dashed curve in Fig. 7) who derived the following relation between the ratio  $R_{SM}$  and the ratio of the electric and magnetic neutron form factors:

$$R_{SM}(Q^2) = \frac{M_N k_\Delta(Q^2) G_E^n(Q^2)}{2 Q^2 G_M^n(Q^2)}. \quad (50)$$

For  $Q^2 > 1 \text{ GeV}^2$  our MAID2007 analysis for  $R_{SM}$  disagrees with the JLab analysis of Aznauryan et al. [63]. Whereas our analysis stays almost constant, the JLab analysis suggests a much larger negative slope. We note that we had obtained a similar slope in our previous MAID2003 analysis [60]. However, while repeating the data analysis at  $Q^2 = 5$  and  $6 \text{ GeV}^2$  in different energy ranges, we found a strong dependence of the fit on the energy interval used. Whereas our results of 2007 were obtained with the full energy range of  $W = (1110 - 1390) \text{ MeV}$ , Fig. 7 also shows an analysis (blue open circles) in the energy range of  $W = 1200 - 1260 \text{ MeV}$ , much closer to the resonance energy. If we choose the energy interval even closer to resonance,  $W = 1220 - 1240 \text{ MeV}$ , the errors increase further by a factor of 2 and the  $E/M$  ratio becomes large and positive, while the  $S/M$  ratio remains the same. We conclude that the analysis in this  $Q^2$  range strongly depends on the energy interval and the parametrization of the background used in the analysis and requires further studies. In order to solve this problem it may be necessary to obtain higher statistics in the data or to measure additional polarization observables, such as recoil polarization. The same conclusion is also likely for the highest  $Q^2$  values that were analyzed with the data of Villano et al. [34] at  $Q^2$  values of 6.3 and 7.6  $\text{GeV}^2$ . For these data we

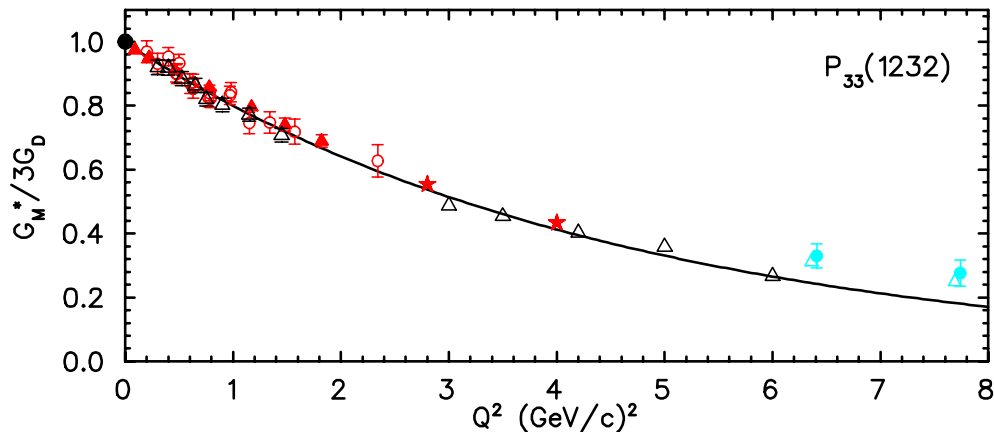


**Fig. 5.** The  $Q^2$  dependence of the magnetic form factor  $G_M^*$  for the  $N\Delta(1232)$  transition divided by  $3G_D(Q^2)$  in the definition of Ash [5]. The curve shows the result of our MAID2007 fit with Eq. (47). The black solid circle at  $Q^2 = 0$  shows the result of the Mainz photoproduction experiment [24] and is practically equal to 1.0, the red data points are from Refs. [9] for solid triangles, [6] for open circles and [25] for solid stars. The black open triangles show the new JLab analysis of Aznauryan et al. [63]. The cyan open triangles and solid circles show the isobar analysis of Ref. [34] and our own new analysis, respectively.

obtain a  $G_M^*$  form factor consistent with the JLab analysis. However, these fits yield values about 30-50% higher than our global fit to the world data.

## 4.2 Second Resonance Region

Above the two-pion threshold, we can no longer apply the two-channel unitarity and consequently the Watson theorem does not hold anymore. Therefore, the background amplitude of the partial waves does not vanish at resonance as is the case for the  $\Delta(1232)$ . As an immediate consequence the resonance-background separation becomes model-dependent. In MAID2007 we choose to separate the background and resonance contributions according to the K-matrix approximation, Eqs. (18,19). Furthermore, we recall that the absolute values of the helicity amplitudes are correlated with the input used for the total resonance width  $\Gamma_R$  and the single-pion branching ratio  $\beta_\pi$ , which gives rise to additional uncertainties from these hadronic resonance parameters. On the experimental side, the data at the higher energies are no longer as abundant as in the  $\Delta$  region. However, the large data set recently obtained mainly by the CLAS collaboration (see Table 5) enabled us to determine the transverse and longitudinal helicity couplings as functions of  $Q^2$  for all the four-star resonances below 1800 MeV. These data are available in the kinematical regions of  $1100 \text{ MeV} < W < 1680 \text{ MeV}$  and  $0.4 \text{ GeV}^2 < Q^2 < 4.5 \text{ GeV}^2$ .

The helicity amplitudes for the Roper resonance  $P_{11}(1440)$  are displayed in Fig. 8. Our latest  $Q^2$ -dependent solution (solid lines) is in reasonable agreement with the single- $Q^2$  analysis (red circles). The figure shows a zero crossing of the transverse helicity amplitude at  $Q^2 \approx 0.7 \text{ GeV}^2$  and a maximum at the relatively large momentum transfer  $Q^2 \approx 2.0 \text{ GeV}^2$ . The longitudinal Roper excitation rises to large values around  $Q^2 \approx 0.5 \text{ GeV}^2$  and, in fact, produces one of the strongest longitudinal amplitudes we find in our analysis. This answers the question raised by Li and Burkert[88]



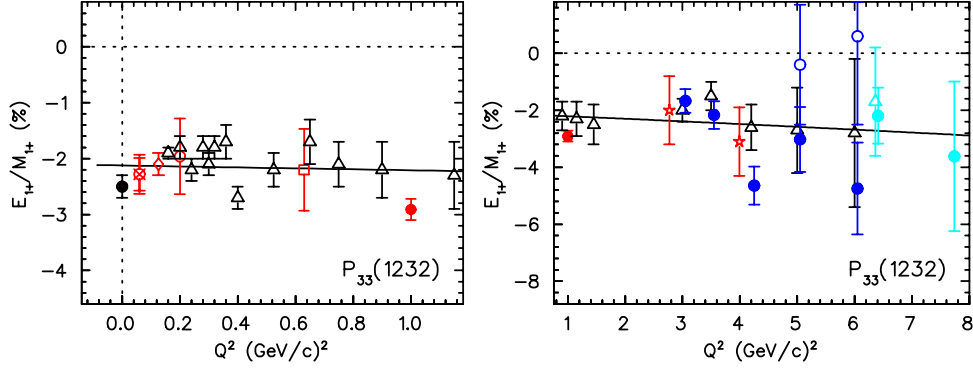


**Fig. 6.** The  $Q^2$  dependence of the ratio  $R_{EM}$  at the  $\Delta(1232)$  resonance. The curve shows the result of our MAID2007 fit with Eq. (47). The black circle at  $Q^2 = 0$  represents the Mainz photoproduction experiment [24]. The red data points are from Refs. [15] (cross), [86] (open circles), [18] (open triangle), [16,17] (open square), [30] (solid circle), and [25] (solid stars). The black open triangles show the new JLab analysis of Aznauryan et al. [63]. The blue solid circles are our 2007 analysis [58] and the blue open circles from our new work discussed in the text. The cyan open triangles and cyan solid circles show the isobar model analysis of Ref. [34] and our own new analysis, respectively.

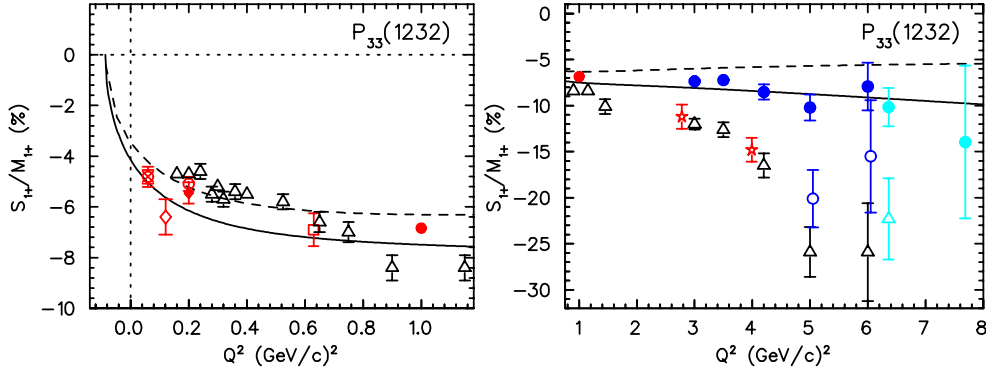


**Fig. 7.** The  $Q^2$  dependence of the ratio  $R_{SM}$  at the  $\Delta(1232)$  resonance position. The solid line shows our MAID2007 fit with Eq. (48) and the dashed curve is the Buchmann prediction relating  $R_{SM}$  to the elastic neutron form factors [85]. The red data points are from Refs. [15] (cross), [13] (open diamond), [14] (solid diamond), [86] (open circles), [16,17] (open square), [30] (solid circle), and [25] (solid stars). The black open triangles show the new JLab analysis of Aznauryan et al. [63], the blue solid circles are our 2007 analysis [58], and the blue open circles result from our new investigation discussed in the text. The cyan open triangles and cyan solid circles show the isobar analysis of Ref. [34] and our new analysis, respectively.

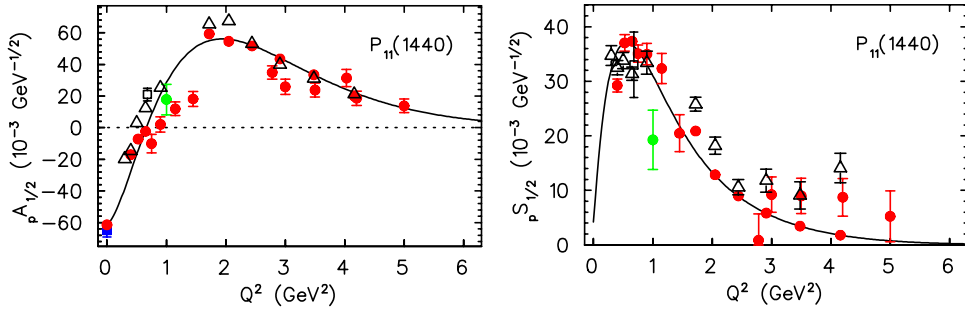


**Fig. 8.** Transverse and longitudinal form factors of the  $P_{11}(1440)$  Roper resonance. The red circles are the MAID analysis of 2007 [58] and 2008, the open black triangles are the 2009 JLab analysis [63] and the open squares are from Ref. [87]. For the transverse form factor at  $Q^2 = 0$  we show the PDG average [1] (blue square) and our MAID2007 result of photoproduction (red circle), which partly overlap here. The green point at  $Q^2 = 1.0$  GeV<sup>2</sup> shows our analysis of the JLab/Hall A data of Laveissiere et al. [26]. The curves show the MAID2008 parametrization. All FF data points analyzed by the MAID group can be downloaded from the MAID website [58].

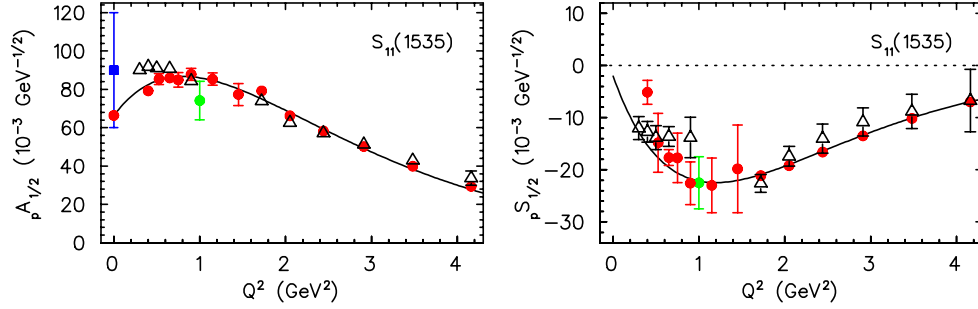


**Fig. 9.** Transverse and longitudinal form factors of the  $S_{11}(1535)$  resonance. The curves show the MAID2007 parametrization. Further notation as in Fig. 8.

whether the Roper resonance is a radially excited 3-quark state or a quark-gluon hybrid, because in the latter case the longitudinal coupling should vanish completely.

Figure 9 displays the results for the  $S_{11}(1535)$  resonance. The red single- $Q^2$  data points show our results of 2007, which are in good agreement with our  $Q^2$ -dependent analysis (solid lines). The black triangles are the 2009 results of Ref. [63]. The blue data point at  $Q^2 = 0$  represents the PDG average over several  $\gamma, \pi$  and  $\gamma, \eta$  analyses. Whereas we find values around 65 in all MAID analyses, the JLab analysis obtains values around 90 for  $\gamma, \pi$  and 110 for  $\gamma, \eta$  [64]. A peculiarity is worth mentioning for the longitudinal form factor. In the long-wavelength limit near pseudothreshold, at  $Q^2 = -(M_R - M_N)^2$  or  $-0.36$  GeV<sup>2</sup> for the  $S_{11}$ , the Siegert theorem predicts a positive value for  $S_{1/2}(Q^2)$  with a positive slope, whereas both the MAID and the JLab groups find negative values for all physical values,  $Q^2 > 0$ .

Whereas the inclusion of the 2008 Park  $\pi^+$  data [33] did not modify our 2007 solution for the  $S_{11}$  resonance, some modifications were necessary for the  $D_{13}(1520)$  resonance shown by the left panels of Fig. 10. For this resonance we find significant

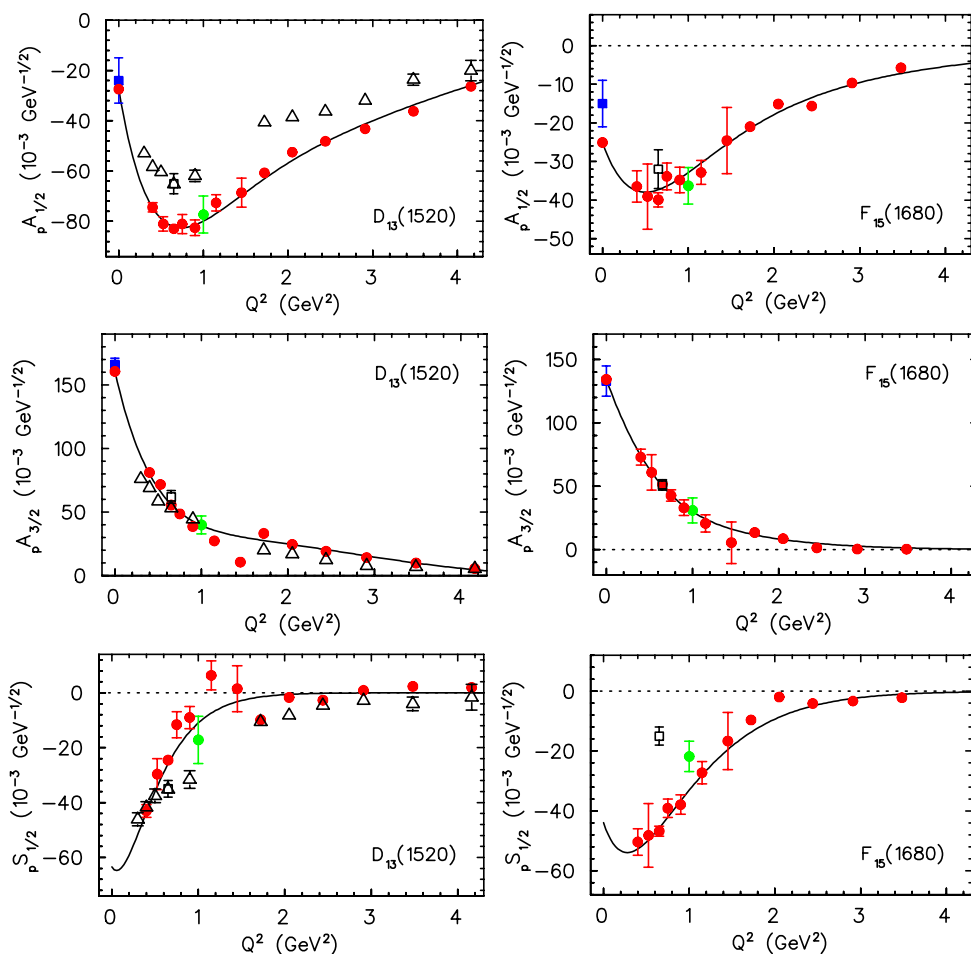


**Fig. 10.** Transverse and longitudinal form factors of the  $D_{13}(1520)$  (left panels) and  $F_{15}(1680)$  (right panels) resonances. The curves show the MAID2008 parametrization. Further notation as in Fig. 8.

deviations in the comparison with the JLab partial wave analysis of 2009, especially for  $A_{1/2}$  over the whole range of  $Q^2$ .

### 4.3 Third Resonance Region

A similar situation as for the  $D_{13}$  resonance is obtained for the  $F_{15}(1680)$  shown in Fig. 10 (right panels). However, there is only one data point at  $Q^2 = 0.65$  GeV<sup>2</sup> from the JLab analysis of  $1\pi - 2\pi$  analysis [87] to be compared which agrees quite well for the transverse form factors but differs significantly for  $S_{1/2}$ . For both of these proton resonances the helicity non-conserving amplitude  $A_{3/2}$  dominates for real photons but, with increasing values of  $Q^2$ , drops much faster than the helicity conserving amplitude  $A_{1/2}$ . As a consequence the asymmetry

$$\mathcal{A}(Q^2) = \frac{|A_{1/2}|^2 - |A_{3/2}|^2}{|A_{1/2}|^2 + |A_{3/2}|^2} \quad (51)$$

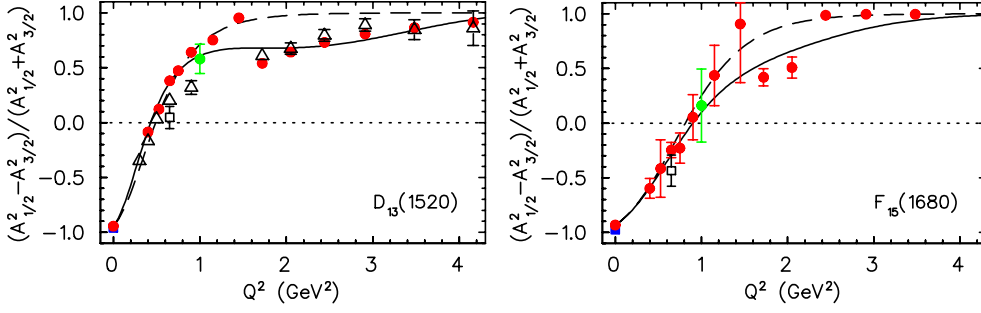


**Fig. 11.** The helicity asymmetry  $\mathcal{A}(Q^2)$  of Eq. (51) for the  $D_{13}(1520)$  and  $F_{15}(1680)$  resonances of the proton. The dashed and solid curves are the MAID2007 and most recent MAID2008 solutions, respectively. Further notation as in Fig. 8.

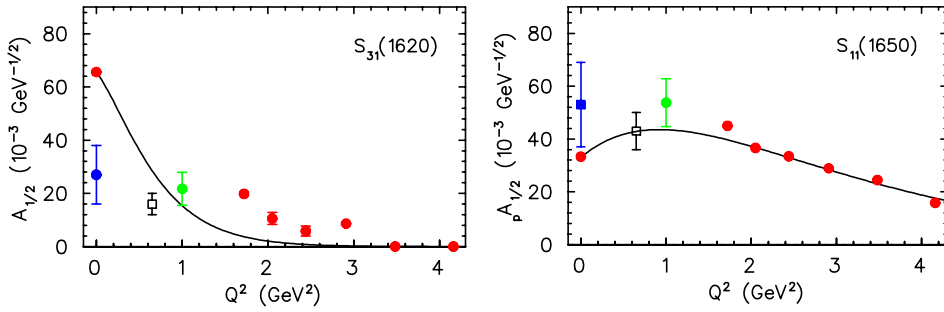


**Fig. 12.** Transverse form factors of the  $S_{31}(1620)$  and  $S_{11}(1650)$  resonances. The curves show the MAID2007 parametrization. Further notation as in Fig. 8.

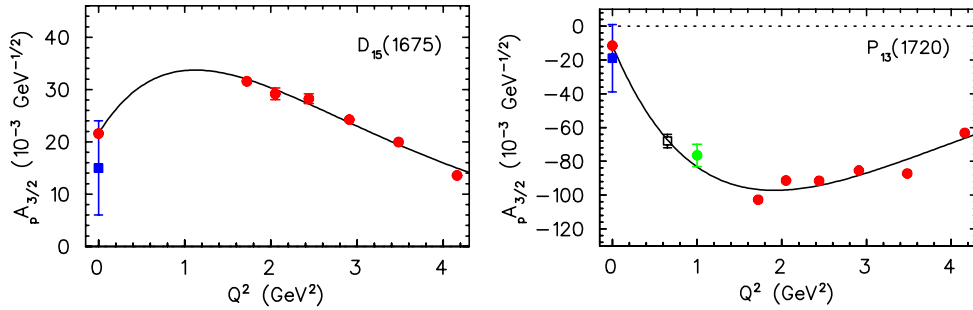


**Fig. 13.** Transverse form factor of the  $D_{15}(1675)$  (left) and  $P_{13}(1720)$  (right) resonance. For these two states the  $A_{1/2}$  form factors are practically zero in the MAID analysis. The curves show the MAID2008 parametrization. Further notation as in Fig. 8.

changes rapidly from values close to  $-1$  to values near  $+1$  over a very small  $Q^2$  range. This behavior has dramatic consequences for  $Q^2$ -dependent sum rules. Whereas we found significant differences between the MAID and JLab analyses for individual form factors, these differences almost disappear in the asymmetries. For comparison, the asymmetry  $\mathcal{A}$  for the  $\Delta(1232)$  resonance takes the value  $\approx -0.5$ , practically constant over the plotted  $Q^2$  range. This is one more indication for the special role of the  $\Delta$  resonance, which ‘does not care’ about the helicity conservation required by asymptotic QCD, at least in the currently available  $Q^2$  range.

The resonances  $S_{31}(1620)$  and  $S_{11}(1650)$  are shown in Fig. 12. The photon couplings of the  $S_{31}$  resonance show a very large spread, see Table 3. Whereas the PDG  $A_{1/2}$  value at the photon point is only  $(27 \pm 11) \cdot 10^{-3} \text{ GeV}^{-1/2}$ , our MAID2007 value is 66 in the same units. In the range  $Q^2 = 1 - 2 \text{ GeV}^2$  we obtain very small values, and for higher  $Q^2$  this amplitude tends towards zero. For the transverse FF of the  $S_{11}(1650)$  resonance we find a solution close to the shape of the first  $S_{11}$  resonance, albeit with a much reduced overall strength. The analysis of the longitudinal FFs leads to very small values for both resonances.

Finally, in Fig. 13 we show the situation for the  $D_{15}(1675)$  and  $P_{13}(1720)$  resonances, both without a significant longitudinal coupling. Unlike the situation discussed before, these two resonances have dominantly helicity  $3/2$  transitions, whereas the  $A_{1/2}$  transition is consistent with zero. As for the  $\Delta(1232)$ , these are further examples for which the pQCD prediction for helicity conservation does not hold in the  $Q^2$  region below  $5 \text{ GeV}^2$ . However, for these resonances our data analysis is at its kinematical limit, we can hardly reach the resonance positions and therefore only the low-energy tails were analyzed.

## 5 Empirical transverse charge transition densities

In this section we consider the e.m.  $N \rightarrow N^*$  transition when viewed from a light front moving towards the baryon. Equivalently, this corresponds to a frame in which the baryons have large momentum components along the  $z$ -axis chosen along the direction of  $P = (p + p')/2$ , where  $p$  ( $p'$ ) are the initial (final) baryon four-momenta. We indicate the baryon light-front ‘plus’ component by  $P^+$  (defining  $a^\pm \equiv a^0 \pm a^3$ ). We can furthermore choose a symmetric frame in which the virtual photon four-momentum  $q$  has  $q^+ = 0$  and a transverse component (in the  $xy$ -plane) indicated by the transverse vector  $\mathbf{q}_\perp$ , satisfying  $q^2 = -\mathbf{q}_\perp^2 \equiv -Q^2$ . In such a symmetric frame, the virtual photon only couples to forward moving partons and the component  $J^+$  of the electromagnetic current can be interpreted as the quark charge density operator. Considering only  $u$  and  $d$  quarks, we have  $J^+(0) = +2/3 \bar{u}(0)\gamma^+u(0) - 1/3 \bar{d}(0)\gamma^+d(0)$ . Each term in this expression is a positive operator since  $\bar{q}\gamma^+q \propto |\gamma^+q|^2$ .

We define a transition charge density for the unpolarized  $N \rightarrow N^*$  transition by the Fourier transform

$$\rho_0^{NN^*}(\mathbf{b}) \equiv \int \frac{d^2\mathbf{q}_\perp}{(2\pi)^2} e^{-i\mathbf{q}_\perp \cdot \mathbf{b}} \frac{1}{2P^+} \langle P^+, \frac{\mathbf{q}_\perp}{2}, \lambda | J^+(0) | P^+, -\frac{\mathbf{q}_\perp}{2}, \lambda \rangle, \quad (52)$$

where  $\lambda$  denotes the nucleon and resonance light-front helicities,  $\mathbf{q}_\perp = Q(\cos\phi_q \hat{e}_x + \sin\phi_q \hat{e}_y)$ , and the 2-dimensional vector  $\mathbf{b}$  points to a position in the  $xy$ -plane.

We will consider the cases of  $j = 1/2$  resonances, as  $P_{11}$  and  $S_{11}$ , and of  $j = 3/2$  resonances, as  $P_{33}$  and  $D_{13}$ . For the spin  $1/2$  resonances we can observe monopole and dipole patterns as for the nucleon, but for the spin  $3/2$  resonances, we also obtain quadrupole patterns.

The above unpolarized transition charge density involves only one of the two or three independent  $N \rightarrow N^*$  e.m. form factors and leads to the monopole pattern. To

extract the full information of the  $NN^*$  transition, we consider the transition charge densities for transversely polarized nucleons and resonances.

We denote this transverse polarization direction by  $\mathbf{S}_\perp = \cos \phi_S \hat{e}_x + \sin \phi_S \hat{e}_y$ . The transverse spin state can be expressed in terms of the light front helicity spinors as  $|s_\perp = +\frac{1}{2}\rangle = (|\lambda = +\frac{1}{2}\rangle + e^{i\phi_S} |\lambda = -\frac{1}{2}\rangle) / \sqrt{2}$ , with  $s_\perp$  the nucleon spin projection along the direction of  $\mathbf{S}_\perp$ .

We can then define a transition charge density for transversely polarized  $N$  and  $N^*$ , both along the direction of  $\mathbf{S}_\perp$  as

$$\rho_T^{NN^*}(\mathbf{b}) \equiv \int \frac{d^2 \mathbf{q}_\perp}{(2\pi)^2} e^{-i \mathbf{q}_\perp \cdot \mathbf{b}} \frac{1}{2P^+} \langle P^+, \frac{\mathbf{q}_\perp}{2}, s'_\perp | J^+(0) | P^+, -\frac{\mathbf{q}_\perp}{2}, s_\perp \rangle. \quad (53)$$

The nonsymmetric pattern, which describes the deviation from the circular symmetric unpolarized charge density, depends on the orientation of  $\mathbf{b} = b(\cos \phi_b \hat{e}_x + \sin \phi_b \hat{e}_y)$ . In the following we choose the transverse spin along the  $x$ -axis ( $\phi_S = 0$ ).

In general we can write the transition densities in the following way for  $j = 1/2$  and  $j = 3/2$  states:

$$\rho_T^{NN^*}(\mathbf{b}) = \rho_0^{NN^*}(b) + \sin(\phi_b - \phi_S) \rho_1^{NN^*}(b) + \cos 2(\phi_b - \phi_S) \rho_2^{NN^*}(b). \quad (54)$$

For a comparison we first consider the transverse charge densities in a nucleon [75], ( $j^\pi = 1/2^+$ ,  $s_\perp = s'_\perp = +\frac{1}{2}$ ,  $\rho_2 \equiv 0$ ),

$$\rho_0^N(b) = \int_0^\infty \frac{dQ}{2\pi} Q J_0(bQ) F_1^N(Q^2), \quad (55)$$

$$\rho_1^N(b) = \int_0^\infty \frac{dQ}{2\pi} Q J_1(bQ) \frac{Q}{2M_N} F_2^N(Q^2), \quad (56)$$

where  $F_1, F_2$  are the usual Dirac form factors of the nucleon.

For the transverse charge densities in the nucleon to Roper transition [89], ( $j^\pi = 1/2^+$ ,  $s_\perp = s'_\perp = +\frac{1}{2}$ ,  $\rho_2 \equiv 0$ ), we get

$$\rho_0^{NP_{11}}(b) = \int_0^\infty \frac{dQ}{2\pi} Q J_0(bQ) F_1^{NP_{11}}(Q^2), \quad (57)$$

$$\rho_1^{NP_{11}}(b) = \int_0^\infty \frac{dQ}{2\pi} Q J_1(bQ) \frac{Q}{(M_R + M_N)} F_2^{NP_{11}}(Q^2), \quad (58)$$

where  $F_1, F_2$  are related to the helicity transition form factors  $A_{1/2}(Q^2)$  and  $S_{1/2}(Q^2)$  in the following way

$$F_1^{NP_{11}}(Q^2) = \frac{1}{N_-} \frac{Q^2}{Q_+^2} (A_{1/2} + \frac{\sqrt{2}(M_R + M_N)}{k_R} S_{1/2}), \quad (59)$$

$$F_2^{NP_{11}}(Q^2) = \frac{1}{N_-} \frac{Q^2}{Q_+^2} (\frac{(M_R + M_N)^2}{Q^2} A_{1/2} - \frac{\sqrt{2}(M_R + M_N)}{k_R} S_{1/2}). \quad (60)$$

For the transverse charge densities in the nucleon to  $S_{11}(1535)$  transition, ( $j^\pi = 1/2^-$ ,  $s_\perp = -s'_\perp = +\frac{1}{2}$ ,  $\rho_2^N \equiv 0$ ), we get

$$\rho_0^{NS_{11}}(b) = \int_0^\infty \frac{dQ}{2\pi} Q J_0(bQ) F_1^{NS_{11}}(Q^2), \quad (61)$$

$$\rho_1^{NS_{11}}(b) = - \int_0^\infty \frac{dQ}{2\pi} Q J_1(bQ) \frac{Q}{(M_R + M_N)} F_2^{NS_{11}}(Q^2), \quad (62)$$

where  $F_1, F_2$  are related to the transition form factors  $A_{1/2}(Q^2)$  and  $S_{1/2}(Q^2)$  in the following way

$$F_1^{NS_{11}}(Q^2) = \frac{1}{N_+} \frac{Q^2}{Q_-^2} \left( A_{1/2} - \frac{\sqrt{2}(M_R - M_N)}{k_R} S_{1/2} \right), \quad (63)$$

$$F_2^{NS_{11}}(Q^2) = \frac{1}{N_+} \frac{Q^2}{Q_-^2} \left( \frac{(M_R^2 - M_N^2)}{Q^2} A_{1/2} + \frac{\sqrt{2}(M_R + M_N)}{k_R} S_{1/2} \right). \quad (64)$$

For the transverse charge densities in the nucleon to  $\Delta(1232)P_{33}$  transition [75], ( $j^\pi = 3/2^+$ ,  $s_\perp = s'_\perp = +\frac{1}{2}$ ), we get

$$\rho_0^{N\Delta}(b) = \int_0^\infty \frac{dQ}{2\pi} Q J_0(bQ) \frac{1}{2} G_{+\frac{1}{2}+\frac{1}{2}}^+(Q^2), \quad (65)$$

$$\rho_1^{N\Delta}(b) = - \int_0^\infty \frac{dQ}{2\pi} Q J_1(bQ) \frac{1}{2} \left[ \sqrt{3} G_{+\frac{3}{2}+\frac{1}{2}}^+(Q^2) + G_{+\frac{1}{2}-\frac{1}{2}}^+(Q^2) \right], \quad (66)$$

$$\rho_2^{N\Delta}(b) = - \int_0^\infty \frac{dQ}{2\pi} Q J_2(bQ) \frac{1}{2} \sqrt{3} G_{+\frac{3}{2}-\frac{1}{2}}^+(Q^2), \quad (67)$$

where

$$\begin{aligned} G_{+\frac{1}{2}+\frac{1}{2}}^+ &= \frac{-1}{4} \frac{(M_\Delta + M_N)}{M_N} \frac{Q^2}{Q_+^2} \left\{ G_M^* \right. \\ &\quad \left. + G_E^* \frac{3}{Q_-^2} [(3M_\Delta + M_N)(M_\Delta - M_N) - Q^2] \right. \\ &\quad \left. + 2G_C^* \left[ -\frac{(M_\Delta + M_N)}{M_\Delta} + \frac{3Q^2}{Q_-^2} \right] \right\}, \end{aligned} \quad (68)$$

$$\sqrt{3} G_{+\frac{3}{2}+\frac{1}{2}}^+ + G_{+\frac{1}{2}-\frac{1}{2}}^+ = \frac{(M_\Delta + M_N)}{M_N} \frac{Q}{Q_+^2} \left\{ G_M^*(M_\Delta + M_N) + G_C^* \frac{Q^2}{2M_\Delta} \right\}, \quad (69)$$

$$\begin{aligned} G_{+\frac{3}{2}-\frac{1}{2}}^+ &= \frac{\sqrt{3}}{4} \frac{(M_\Delta + M_N)}{M_N} \frac{Q^2}{Q_+^2} \left\{ G_M^* \right. \\ &\quad \left. + G_E^* \left[ 1 - \frac{4M_\Delta(M_\Delta - M_N)}{Q_-^2} \right] - G_C^* \frac{2Q^2}{Q_-^2} \right\}. \end{aligned} \quad (70)$$

Finally, we obtain for the transverse charge densities in the nucleon to  $D_{13}(1520)$  transition, ( $j^\pi = 3/2^-$ ,  $s_\perp = -s'_\perp = +\frac{1}{2}$ ),

$$\rho_0^{ND_{13}}(b) = \int_0^\infty \frac{dQ}{2\pi} Q J_0(bQ) \frac{1}{2} G_{+\frac{1}{2}+\frac{1}{2}}^+(Q^2), \quad (71)$$

$$\rho_1^{ND_{13}}(b) = \int_0^\infty \frac{dQ}{2\pi} Q J_1(bQ) \frac{1}{2} \left[ \sqrt{3} G_{+\frac{3}{2}+\frac{1}{2}}^+(Q^2) + G_{-\frac{1}{2}+\frac{1}{2}}^+(Q^2) \right], \quad (72)$$

$$\rho_2^{ND_{13}}(b) = \int_0^\infty \frac{dQ}{2\pi} Q J_2(bQ) \frac{1}{2} \sqrt{3} G_{-\frac{3}{2}+\frac{1}{2}}^+(Q^2), \quad (73)$$

where

$$G_{+\frac{1}{2}+\frac{1}{2}}^+ = \frac{1}{\sqrt{6}} \frac{Q^2}{Q_+^2} \left\{ -F_1^{ND_{13}} - \frac{1}{2} F_2^{ND_{13}} + \frac{(M_R + M_N)}{M_R} F_3^{ND_{13}} \right\}, \quad (74)$$

$$G_{+\frac{3}{2}+\frac{1}{2}}^+ = \frac{1}{\sqrt{2}} \frac{QM_R}{Q_+^2} \left\{ F_1^{ND_{13}} + \frac{(M_R + M_N)}{2M_R} F_2^{ND_{13}} \right\}, \quad (75)$$

$$G_{-\frac{1}{2}+\frac{1}{2}}^+ = \frac{1}{\sqrt{6}} \frac{QM_N}{Q_+^2} \left\{ -F_1^{ND_{13}} - \frac{(M_R + M_N)}{2M_N} F_2^{ND_{13}} - \frac{Q^2}{M_R M_N} F_3^{ND_{13}} \right\}, \quad (76)$$

$$G_{-\frac{3}{2}+\frac{1}{2}}^+ = \frac{1}{2\sqrt{2}} \frac{Q^2}{Q_+^2} F_2^{ND_{13}}, \quad (77)$$

and

$$F_1^{ND_{13}} = \frac{\sqrt{2}}{N_+} \frac{Q_+^2}{Q_-^2} \left\{ A_{3/2} - \sqrt{3} A_{1/2} \right\}, \quad (78)$$

$$F_2^{ND_{13}} = \frac{\sqrt{2}}{N_+} \frac{1}{Q_-^2} \left\{ (M_R^2 - M_N^2 - Q^2) \left[ A_{3/2} + \sqrt{3} A_{1/2} \right] - \sqrt{\frac{3}{2}} \frac{4M_R Q^2}{k_R} S_{1/2} \right\} - F_1^{ND_{13}}, \quad (79)$$

$$F_3^{ND_{13}} = -\frac{\sqrt{2}}{N_+} \frac{2M_R^2}{Q_-^2} \left\{ A_{3/2} + \sqrt{3} A_{1/2} + \frac{\sqrt{6}}{2M_R k_R} (M_R^2 - M_N^2 - Q^2) S_{1/2} \right\}. \quad (80)$$

Throughout these definitions we have used the abbreviations

$$Q_{\pm}^2 = (M_R \pm M_N)^2 + Q^2, \quad (81)$$

$$N_{\pm} = \sqrt{\frac{\pi \alpha Q_{\pm}^2}{M_R M_N \kappa_R}}, \quad (82)$$

and  $k_R = Q_+ Q_- / (2M_R)$  for the  $Q^2$ -dependent virtual photon momentum at  $W = M_R$ , which is equal to the equivalent photon energy  $\kappa_R$  at  $Q^2 = 0$ .

In Figs. 14 and 15 we map the results for the  $N \rightarrow P_{11}(1440)$  transition charge densities for protons and neutrons, respectively. The left panels show the unpolarized case, the right panels are obtained for transverse polarization of the nucleon and the Roper. For the transition on a proton, which is well constrained by the data, we use the MAID2008 parametrization and find an inner region of positive quark charge concentrated within 0.4 fm, accompanied by a relatively broad band of negative charge extending out to about 0.8 fm.

For transversely polarized baryons, the large magnetic transition strength at the real photon point yields a sizeable shift of the charge distribution which induces an electric dipole moment. For the neutron, which is not so very well constrained by the data, the MAID2007 analysis yields charge distributions of opposite sign compared to the proton, with the active quarks spreading out over even larger spatial distances.

Figure 16 shows the unpolarized and polarized transition charge densities from the proton to the  $S_{11}(1535)$  resonance. Comparing these results to the corresponding Fig. 14 for the Roper, we find that the u and d quarks are similarly distributed in the unpolarized densities but the dipole contribution to the polarized densities is much less pronounced for the  $S_{11}$  due to the much smaller  $F_2^{NN^*} / F_1^{NN^*}$  form factor ratio.

In the last two figures, we show the transition densities to the  $j = 3/2$  resonances  $\Delta(1232)$  and  $D_{13}(1520)$ . For both transitions we obtain three multipole patterns, monopole, dipole, and quadrupole, which add to the polarized transition density, according Eq. (54). For the  $p \rightarrow \Delta(1232)$  transition in Fig. 18 we show the unpolarized and polarized transition densities as for the previous cases. In addition we also present the quadrupole pattern alone, which has a very small magnitude due to the suppressed  $E2, C2$  admixtures in the  $N\Delta$  transition. Therefore it cannot be seen in the combined polarized density.



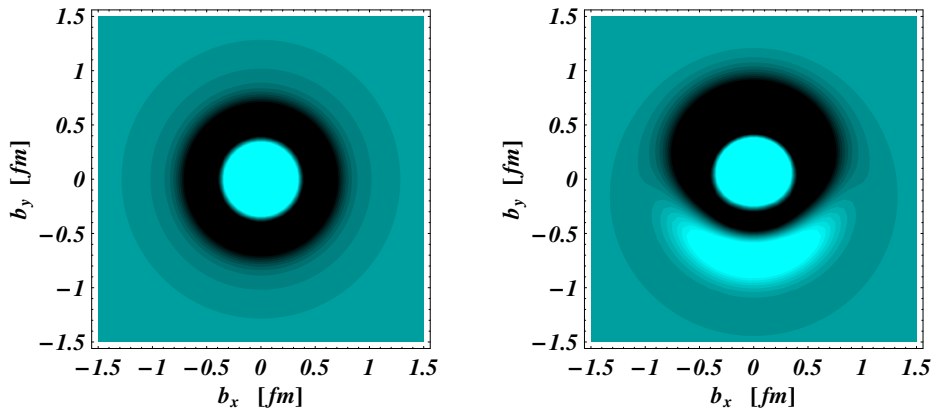


**Fig. 14.** Quark transverse charge density corresponding to the  $p \rightarrow P_{11}(1440)$  e.m. transition. Left panel:  $p$  and  $P_{11}$  are unpolarized ( $\rho_0^{pP_{11}}$ ). Right panel:  $p$  and  $P_{11}$  are polarized along the  $x$ -axis ( $\rho_T^{pP_{11}}$ ). The light (dark) regions correspond to positive (negative) densities. For the  $p \rightarrow P_{11}(1440)$  e.m. transition FFs, we use the MAID2008 parametrization.

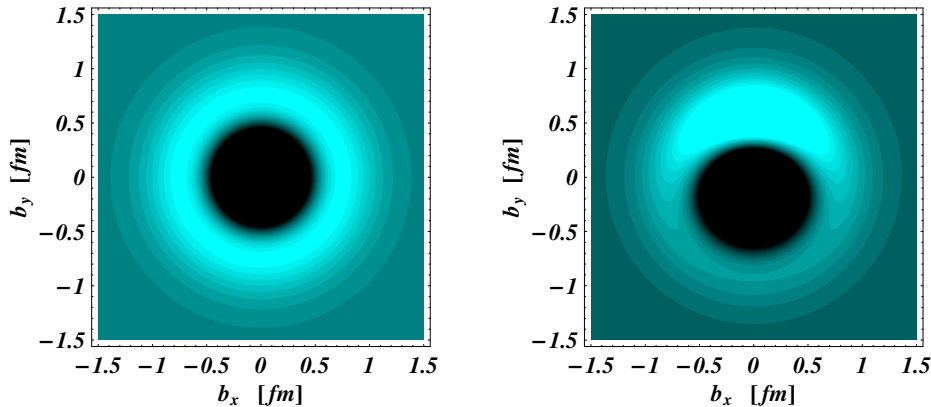


**Fig. 15.** Quark transverse charge density corresponding to the  $n \rightarrow P_{11}(1440)$  e.m. transition. Left panel:  $n$  and  $P_{11}$  are unpolarized ( $\rho_0^{nP_{11}}$ ). Right panel:  $n$  and  $P_{11}$  are polarized along the  $x$ -axis ( $\rho_T^{nP_{11}}$ ). The light (dark) regions correspond to positive (negative) densities. For the  $n \rightarrow P_{11}(1440)$  e.m. transition FFs, we use the MAID2007 parametrization.

Finally, for the  $p \rightarrow D_{13}(1520)$  transition in Fig. 19 we show again the unpolarized density and the polarized density containing all 3 patterns. The unpolarized or monopole density of  $p \rightarrow D_{13}$  shows a more concentrated central positive charge for  $b < 0.3$  fm and a broad ring of negative charges up to  $b \approx 1$  fm. Compared to the Roper and  $S_{11}$  monopole densities the boundaries between u and d quarks are more diffuse for the  $D_{13}(1520)$ . In contrast to the  $N\Delta$  transition, here the quadrupole pattern is much more dominant and shows up clearly in the polarized density, where also the dipole pattern has a significant influence.

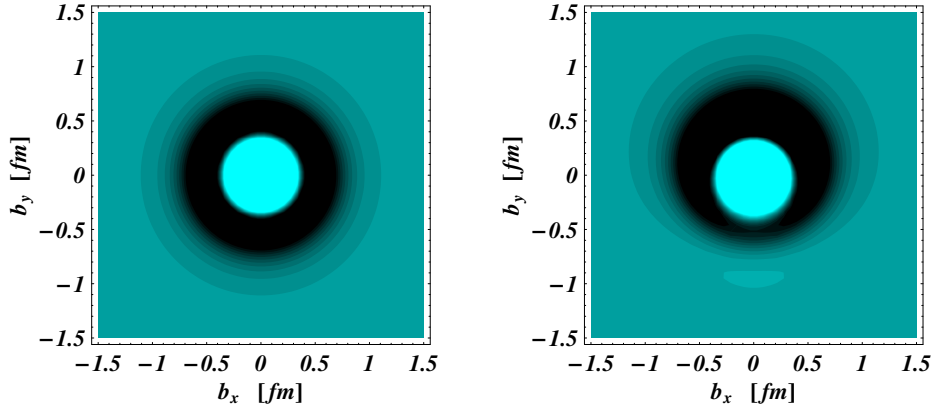


**Fig. 16.** Quark transverse charge density corresponding to the  $p \rightarrow S_{11}(1535)$  e.m. transition. Left panel:  $p$  and  $S_{11}$  are in a light-front helicity  $+1/2$  state ( $\rho_0^{pS_{11}}$ ). Right panel:  $p$  and  $S_{11}$  are polarized along the  $x$ -axis with opposite spin projections ( $\rho_T^{pS_{11}}$ ), i.e.,  $s_{\perp} = -s'_{\perp} = +1/2$ . The light (dark) regions correspond to positive (negative) densities. For the  $p \rightarrow S_{11}(1535)$  e.m. transition FFs, we use the MAID2007 parametrization.

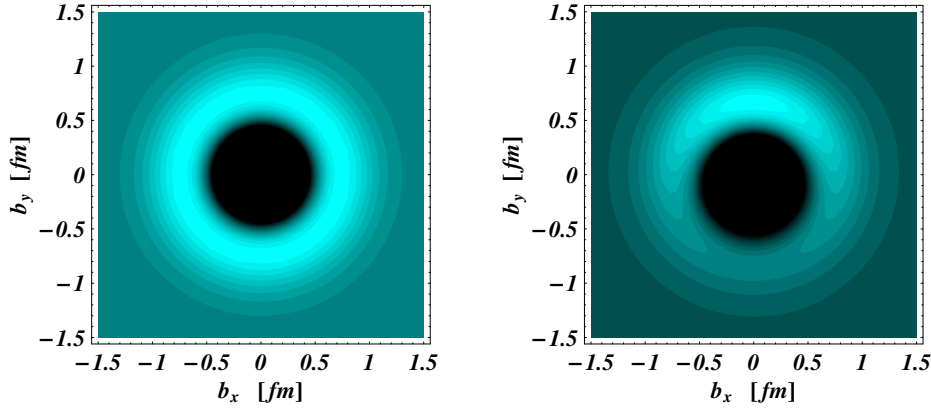


**Fig. 17.** Quark transverse charge density corresponding to the  $n \rightarrow S_{11}(1535)$  e.m. transition. Notation as in Fig. 16.

## 6 Summary and Conclusions

For a complete understanding of the nucleon structure it is prerequisite to know both the ground state form factors and the excitation spectrum, in particular, the transition form factors from the ground state to all the excited states. Among all  $N^*$  and  $\Delta$  resonances listed in PDG, the four-star nucleon resonances are the relevant states that determine the response of the nucleon to electromagnetic probes as photons and electrons.

Using the world database of pion photo- and electroproduction as well as recent data from Mainz, Bonn, Bates, and JLab we have extracted all longitudinal and transverse helicity amplitudes of nucleon resonance excitation for the four-star resonances below  $W = 1.8$  GeV. For this purpose we have extended our unitary isobar model

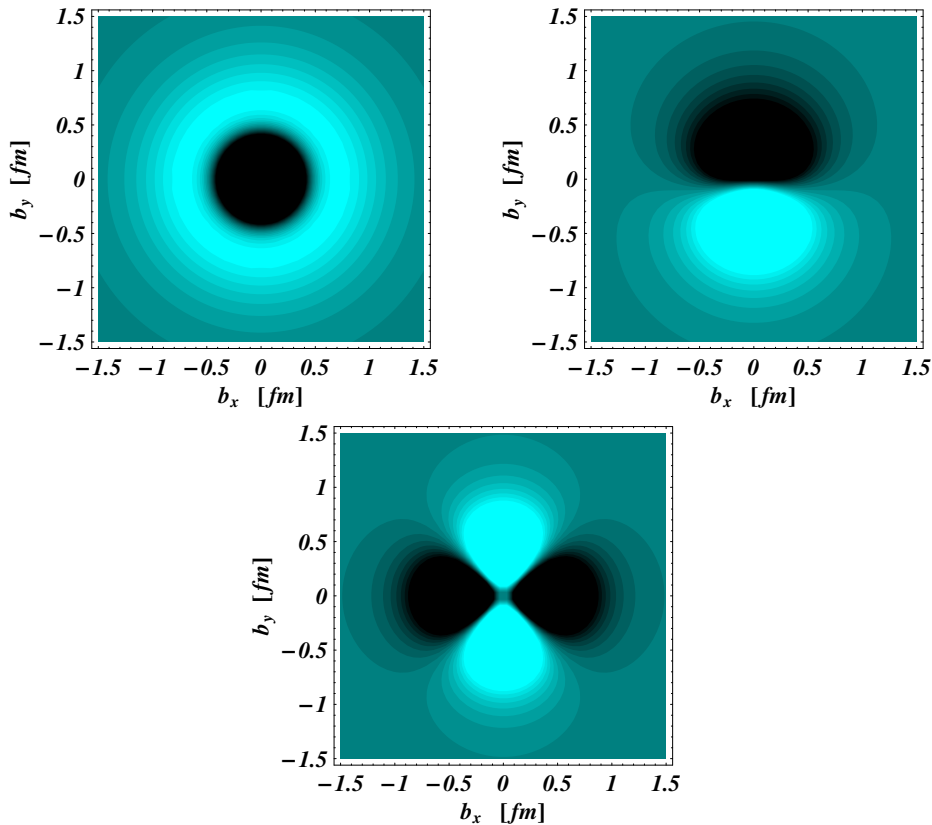


**Fig. 18.** Quark transverse charge density corresponding to the  $p \rightarrow \Delta(1232)P_{33}$  e.m. transition. Upper left panel:  $p$  and  $\Delta$  are in a light-front helicity  $+1/2$  state ( $\rho_0^{pP_{33}}$ ). Upper right panel:  $p$  and  $\Delta$  are polarized along the  $x$ -axis ( $\rho_T^{pP_{33}}$ ) as in Fig. 14. The lower panel shows the quadrupole pattern, whose contribution to the polarized transition density is very small due to the weak  $E2/C2$  admixtures in the  $N\Delta$  transition and practically invisible in the upper right panel. The light (dark) regions correspond to positive (negative) densities. For the  $p \rightarrow P_{33}(1232)$  e.m. transition FFs, we use the MAID2007 parametrization.

MAID, in particular, by parameterizing the  $Q^2$  dependence of the transition amplitudes in more detail. The comparison between single- $Q^2$  fits and overall  $Q^2$ -dependent fits gives us confidence in the determination of the transverse and longitudinal helicity form factors for the resonances  $P_{33}(1232)$ ,  $P_{11}(1440)$ ,  $S_{11}(1535)$ ,  $D_{13}(1520)$ , and  $F_{15}(1680)$ , even though the model uncertainty of the longitudinal amplitudes can be as large as 50% for the  $D_{13}$  and  $F_{15}$ . Similar model uncertainties can be expected for transverse transition form factors of the resonances  $S_{31}(1620)$ ,  $S_{11}(1650)$ ,  $D_{15}(1675)$ , and  $P_{31}(1720)$ , which we analyzed for the first time.

Sufficient reliable form factors exist for the excitation of the resonances  $P_{33}(1232)$ ,  $P_{11}(1440)$ ,  $S_{11}(1535)$ , and  $D_{13}(1520)$ , from which we extract the quark transverse charge densities inducing these transitions. The rings of up and down quarks in these two-dimensional representations show distinctly different angular (multipole) and radial structures which characterize the individual nucleon resonances in a rather lucid way.

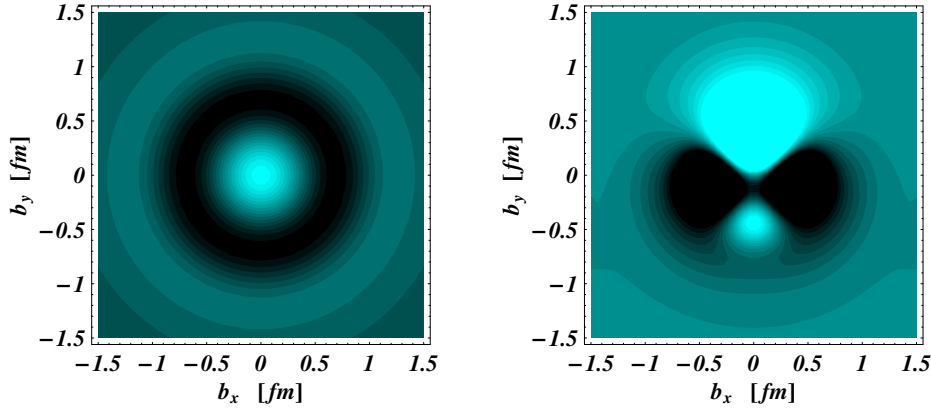


**Fig. 19.** Quark transverse charge density corresponding to the  $p \rightarrow D_{13}(1520)$  e.m. transition. Left panel:  $p$  and  $D_{13}$  are in a light-front helicity  $+1/2$  state ( $\rho_0^{pD_{13}}$ ). Right panel:  $p$  and  $D_{13}$  are polarized along the  $x$ -axis with spin projections ( $\rho_T^{pD_{13}}$ ) as in Fig. 16. The light (dark) regions correspond to positive (negative) densities. For the  $p \rightarrow D_{13}(1520)$  e.m. transition FFs, we use the MAID2008 parametrization.

For further improvement a model-independent partial wave analysis for pion, eta and kaon photoproduction is currently in preparation. First data using beam, target and recoil polarization in various combinations are already taken. Similar to the analysis of the  $P_{33}$  partial waves that allowed us to get model-independent  $\Delta(1232)$  resonance parameters, we will obtain values for all transverse form factors at  $Q^2 = 0$  with high statistical precision and small model dependence. For longitudinal form factors we can not get experimental information at  $Q^2 = 0$ , therefore it is important to perform dedicated experiments in  $(e, e'\pi)$  and  $(e, e'\eta)$  for very low  $Q^2$ . At MAMI such experiments are proposed for the next few years, where longitudinal transition form factors will be studied for  $Q^2 \approx 0.05 \text{ GeV}^2$ . Without this knowledge the longitudinal form factors will always remain very uncertain in the low- $Q^2$  region. At large  $Q^2$  both longitudinal and transverse form factors will be further investigated at JLab, where photon virtualities of  $Q^2$  up to  $12 \text{ GeV}^2$  will soon be available.

We want to thank the Deutsche Forschungsgemeinschaft for the support by the Collaborative Research Center 443 (SFB 443).

## References

1. K. Nakamura et al. (Particle Data Group), J. Phys. G **37** (2010) 075021.
2. G. Y. Chen, S. S. Kamalov, S. N. Yang, D. Drechsel, L. Tiator, Phys. Rev. **C76** (2007) 035206.
3. L. Tiator, S. S. Kamalov, S. Ceci, G. Y. Chen, D. Drechsel, A. Svarc, S. N. Yang, Phys. Rev. **C82** (2010) 055203.
4. R. C. E. Devenish, T. S. Eizenschitz, J. G. Körner, Phys. Rev. **D14** (1976) 3063.
5. W. W. Ash et al., Phys. Lett. B **24** (1967) 165.
6. W. Bartel et al., Phys. Lett. **28B** (1968) 148
7. K. Baetzner, U. Beck, K. H. Becks, C. Berger, J. Drees, G. Knop, M. Leenen, K. Moser et al., Phys. Lett. **B39** (1972) 575-578.

8. J. C. Alder, F. W. Brasse, E. Chazelas, W. Fehrenbach, W. Flauger, K. H. Frank, E. Ganssauge, J. Gayler et al., Nucl. Phys. **B46** (1972) 573-592.
9. S. Stein et al., Phys. Rev. **D12** (1975) 1884.
10. H. F. Jones and M. D. Scadron, Annals Phys. **81** (1973) 1.
11. P. Stoler, Phys. Rept. **226** (1993) 103-171.
12. L. M. Stuart, P. E. Bosted, L. Andivahis, A. Lung, J. Alster, R. G. Arnold, C. C. Chang, F. S. Dietrich et al., Phys. Rev. **D58** (1998) 032003.
13. Th. Pospischil et al., Phys. Rev. Lett. **86** (2001) 2959.
14. D. Elsner et al., Eur. Phys. J. A **27** (2006) 91.
15. S. Stave et al., Eur. Phys. J. A **30** (2006) 471.
16. R. W. Gothe, Prog. Part. Nucl. Phys. **44** (2000) 185 and T. Bantes and R. W. Gothe, private communication.
17. T. Bantes, PhD thesis, Bonn 2003.
18. C. Mertz et al., Phys. Rev. Lett. **86** (2001) 2963.
19. N. F. Sparveris et al. [ OOPS Collaboration ], Phys. Rev. Lett. **94** (2005) 022003.
20. R. Beck, H. P. Krahn, J. Ahrens, H. J. Arends, G. Audit, A. Braghieri, N. d'Hose, S. J. Hall et al., Phys. Rev. Lett. **78** (1997) 606-609.
21. G. Blanpied, M. Blecher, A. Caracappa, C. Djalali, G. Giordano, K. Hicks, S. Hoblit, M. Khandaker et al., Phys. Rev. Lett. **79** (1997) 4337-4340.
22. O. Hanstein, D. Drechsel, and L. Tiator, Phys. Lett. **B 399** (1997) 13.
23. O. Hanstein, D. Drechsel, and L. Tiator, Nucl. Phys. **A632** (1998) 561.
24. R. Beck et al., Phys. Rev. C **61** (2000) 035204.
25. V. V. Frolov et al., Phys. Rev. Lett. **82** (1999) 45.
26. G. Laveissiere et al., Phys. Rev. C **69** (2004) 045202 and Proc. of NSTAR2001, Mainz, World Scientific 2001, p271.
27. K. Joo et al. [ CLAS Collaboration ], Phys. Rev. Lett. **88** (2002) 122001-1.
28. K. Joo et al. [ CLAS Collaboration ], Phys. Rev. C **68** (2003) 032201.
29. K. Joo et al. [ CLAS Collaboration ], Phys. Rev. C **70** (2004) 042201.
30. J. J. Kelly et al., Phys. Rev. Lett. **95** (2005) 102001 and Phys. Rev. C **75** (2007), 025201.
31. H. Egiyan et al. [ CLAS Collaboration ], Phys. Rev. C **73** (2006) 025204.
32. M. Ungaro et al. [ CLAS Collaboration ], Phys. Rev. Lett. **97** (2006) 112003.
33. K. Park et al. [ CLAS Collaboration ], Phys. Rev. **C77** (2008) 015208.
34. A. N. Villano, P. Stoler, P. E. Bosted, S. H. Connell, M. M. Dalton, M. K. Jones, V. Kubarovskiy, G. S. Adams et al., Phys. Rev. **C80** (2009) 035203.
35. R. A. Arndt, R. L. Workman, Z. Li, L. D. Roper, Phys. Rev. **C42** (1990) 1864-1866.
36. R. A. Arndt, I. I. Strakovsky, R. L. Workman, Phys. Rev. **C53** (1996) 430-440; (SP99 solution of the GW/SAID analysis); <http://gwdac.phys.gwu.edu/>.
37. R. A. Arndt, W. J. Briscoe, I. I. Strakovsky, R. L. Workman, AIP Conf. Proc. **904** (2007) 269-275.
38. G. Penner, U. Mosel, Phys. Rev. **C66** (2002) 055212.
39. V. Shklyar, H. Lenske, U. Mosel, Phys. Lett. **B650** (2007) 172-178.
40. A. V. Anisovich, A. Sarantsev, O. Bartholomy, E. Klempt, V. A. Nikonov, U. Thoma, Eur. Phys. J. **A25** (2005) 427-439.
41. A. V. Anisovich, E. Klempt, V. A. Nikonov, M. A. Matveev, A. V. Sarantsev, U. Thoma, Eur. Phys. J. **A44** (2010) 203-220; <http://pwa.hiskp.uni-bonn.de/>.
42. M. Döring, C. Hanhart, F. Huang, S. Krewald, U. -G. Meissner, Nucl. Phys. **A829** (2009) 170-209.
43. M. Döring, K. Nakayama, Eur. Phys. J. **A43** (2010) 83-105.
44. F. Huang, M. Döring, H. Haberzettl, S. Krewald, K. Nakayama,
45. D. Djukanovic, J. Gegelia, S. Scherer, Phys. Rev. **D76** (2007) 037501.
46. S. Capstick, A. Svarc, L. Tiator, J. Gegelia, M. M. Giannini, E. Santopinto, C. Hanhart, S. Scherer et al., Eur. Phys. J. **A35** (2008) 253-266.
47. J. Gegelia, S. Scherer, Eur. Phys. J. **A44** (2010) 425-430.
48. T. R. Hemmert, B. R. Holstein, J. Kambor, J. Phys. G **G24** (1998) 1831-1859.
49. T. A. Gail, T. R. Hemmert, Eur. Phys. J. **A28** (2006) 91-105.
50. V. Pascalutsa, M. Vanderhaeghen, Phys. Rev. **D73** (2006) 034003.

51. V. Pascalutsa, M. Vanderhaeghen, S. N. Yang, Phys. Rept. **437** (2007) 125-232.
52. S. S. Kamalov, S. N. Yang, D. Drechsel, and L. Tiator Phys. Rev. C **64**, (2001) 032201.
53. S. S. Kamalov, and S. N. Yang, Phys. Rev. Lett. **83**, (1999) 4494.
54. T. Sato and T.-S. H. Lee, Phys. Rev. C **63**, (2001) 055201.
55. B. Julia-Diaz, H. Kamano, T.-S. H. Lee, A. Matsuyama, T. Sato, N. Suzuki, Phys. Rev. **C80** (2009) 025207.
56. N. Suzuki, T. Sato, T.-S. H. Lee, Phys. Rev. **C82** (2010) 045206.
57. D. Drechsel, O. Hanstein, S. S. Kamalov, and L. Tiator, Nucl. Phys. A **645** (1999) 145.
58. D. Drechsel, S. S. Kamalov, and L. Tiator, Eur. Phys. J. A **34** (2007) 69;  
<http://www.kph.uni-mainz.de/MAID/>.
59. L. Tiator, D. Drechsel, S. S. Kamalov, M. M. Giannini, E. Santopinto, A. Vassallo, Eur. Phys. J. **A19** (2004) 55-60.
60. L. Tiator, D. Drechsel, S. S. Kamalov, S. N. Yang, Eur. Phys. J. **A17** (2003) 357-363.
61. L. Tiator, D. Drechsel, S. S. Kamalov, and M. Vanderhaeghen, CPC(HEP & NP) **33** (2009) 1051.
62. I. G. Aznauryan et al. [ CLAS Collaboration ], Phys. Rev. **C78** (2008) 045209.
63. I. G. Aznauryan et al. [ CLAS Collaboration ], Phys. Rev. **C80** (2009) 055203.
64. I. Aznauryan, V. D. Burkert, T.-S. H. Lee, V. Mokeev, [arXiv:1102.0597 [nucl-ex]].
65. C. Alexandrou, G. Koutsou, J. W. Negele, Y. Proestos, A. Tsapalis, Phys. Rev. **D83** (2011) 014501.
66. C. Alexandrou, T. Korzec, G. Koutsou, C. Lorce, J. W. Negele, V. Pascalutsa, A. Tsapalis, M. Vanderhaeghen, Nucl. Phys. **A825** (2009) 115-144.
67. H.-W. Lin, S. D. Cohen, R. G. Edwards, D. G. Richards, Phys. Rev. **D78** (2008) 114508.
68. V. M. Braun, M. Göckeler, R. Horsley, T. Kaltenbrunner, A. Lenz, Y. Nakamura, D. Pleiter, P. E. L. Rakow et al., Phys. Rev. Lett. **103** (2009) 072001.
69. D. Drechsel, L. Tiator, Ann. Rev. Nucl. Part. Sci. **54** (2004) 69-114.
70. B. Pasquini, D. Drechsel, L. Tiator, Eur. Phys. J. **A23** (2005) 279-289.
71. B. Pasquini, D. Drechsel, L. Tiator, Eur. Phys. J. **A27** (2006) 231-242.
72. B. Pasquini, D. Drechsel, L. Tiator, Eur. Phys. J. **A34** (2007) 387-403.
73. B. Pasquini, D. Drechsel, M. Vanderhaeghen, [arXiv:1105.4454 [hep-ph]].
74. G. A. Miller, Phys. Rev. Lett. **99** (2007) 112001.
75. C. E. Carlson and M. Vanderhaeghen, Phys. Rev. Lett. **100** (2008) 032004.
76. C. E. Carlson and M. Vanderhaeghen, Eur. Phys. J. A **41** (2009) 1.
77. K. I. Hikasa et al. (Particle Data Group), Phys. Rev. D **45**, (1992) S1.
78. R. Workman, Phys. Rev. **C59** (1999) 3441-3443.
79. V. Bernard, N. Kaiser, J. Gasser, U. G. Meissner, Phys. Lett. **B268** (1991) 291-295.
80. S. S. Kamalov, G.-Y. Chen, S.-N. Yang, D. Drechsel, L. Tiator, Phys. Lett. **B522** (2001) 27-36.
81. M. Dugger et al. [ CLAS Collaboration ], Phys. Rev. **C79** (2009) 065206.
82. R. A. Arndt, W. J. Briscoe, I. I. Strakovsky, R. L. Workman, Phys. Rev. **C66** (2002) 055213.
83. R. A. Arndt, W. J. Briscoe, I. I. Strakovsky, R. L. Workman, Phys. Rev. **C74** (2006) 045205.
84. X.-d. Ji, J.-P. Ma, F. Yuan, Phys. Rev. Lett. **90** (2003) 241601.
85. A. J. Buchmann, Phys. Rev. Lett. **93** (2004) 212301.
86. S. Stave et al. [ A1 Collaboration ], Phys. Rev. **C78** (2008) 025209.
87. I. G. Aznauryan, V. D. Burkert, G. V. Fedotov, B. S. Ishkhanov, V. I. Mokeev, Phys. Rev. **C72** (2005) 045201.
88. Z. P. Li, V. Burkert, and Z. Li, J Phys. Rev. D **46** (1992) 70.
89. L. Tiator, M. Vanderhaeghen, Phys. Lett. B **642** (2009) 344.